Article

Cell

Toward Minimal Residual Disease-Directed Therapy in Melanoma

Graphical Abstract

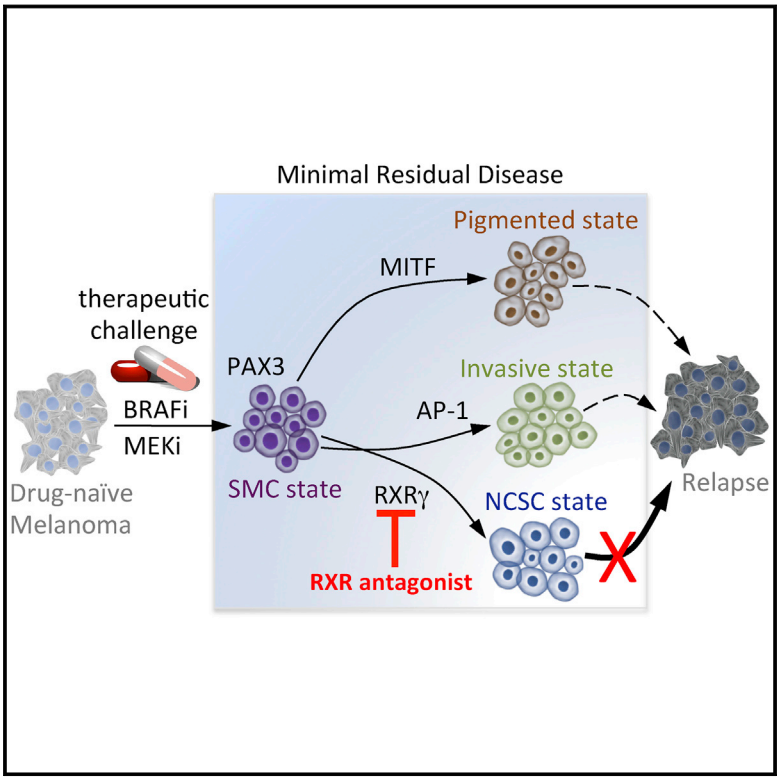

Authors

Florian Rambow, Aljosja Rogiers, Oskar Marin-Bejar, ..., Stein Aerts, Amanda W. Lund, Jean-Christophe Marine

Correspondence

jeanchristophe.marine@kuleuven.vib.be

In Brief

Drug-tolerant cells that persist through treatment of melanoma exhibit multiple transcriptional states, one of which is a key driver that can be targeted therapeutically.

Highlights

- Minimal residual diseases in melanoma exhibit cellular and spatial heterogeneity
- Cell-state transition contributes to co-emergence of distinct drug-tolerant states
- RXR signaling drives emergence of a cell population conferring treatment resistance
- Targeting RXR signaling is promising for delaying or obviating relapse in melanoma

Rambow et al., 2018, Cell *174*, 1–13
August 9, 2018 © 2018 Elsevier Inc.
https://doi.org/10.1016/j.cell.2018.06.025

CellPress

Please cite this article in press as: Rambow et al., Toward Minimal Residual Disease-Directed Therapy in Melanoma, Cell (2018), https://doi.org/10.1016/j.cell.2018.06.025

Article

Cell

Toward Minimal Residual Disease-Directed Therapy in Melanoma

Florian Rambow,[1,2,15] Aljosja Rogiers,[1,2,15] Oskar Marin-Bejar,[1,2] Sara Aibar,[3,4] Julia Femel,[5] Michael Dewaele,[1,2] Panagiotis Karras,[1,2] Daniel Brown,[6] Young Hwan Chang,[7] Maria Debiec-Rychter,[8] Carmen Adriaens,[1,2] Enrico Radaelli,[9] Pascal Wolter,[10] Oliver Bechter,[10] Reinhard Dummer,[11] Mitchell Levesque,[11] Adriano Piris,[12] Dennie T. Frederick,[12] Genevieve Boland,[12] Keith T. Flaherty,[13] Joost van den Oord,[14] Thierry Voet,[6] Stein Aerts,[3,4] Amanda W. Lund,[5] and Jean-Christophe Marine[1,2,16,17,*]

[1]Laboratory for Molecular Cancer Biology, VIB Center for Cancer Biology, KU Leuven, Leuven, Belgium
[2]Department of Oncology, KU Leuven, Leuven, Belgium
[3]Laboratory of Computational Biology, VIB Center for Brain & Disease Research, KU Leuven, Leuven, Belgium
[4]Department of Human Genetics, KU Leuven, Leuven, Belgium
[5]Department of Cell, Developmental, and Cancer Biology, Knight Cancer Institute, Oregon Health and Science University, Portland, OR, USA
[6]Laboratory of reproductive genomics, Department of Human Genetics, KU Leuven, Leuven, Belgium
[7]Department of Biomedical Engineering, Oregon Center for Spatial Systems Biomedicine, Oregon Health and Science University, Portland, OR, USA
[8]Laboratory for Genetics of Malignant Disorders, Department of Human Genetics, KU Leuven, Leuven, Belgium
[9]Comparative Pathology Core, University of Pennsylvania, Department of Pathobiology, Philadelphia, PA, USA
[10]Department of General Medical Oncology, UZ Leuven, Leuven, Belgium
[11]Department of Dermatology, University of Zürich Hospital, Zürich, Switzerland
[12]Department of Surgical Oncology, Massachusetts General Hospital, Boston, MA, USA
[13]Department of Medical Oncology, Massachusetts General Hospital, Boston, MA, USA
[14]Laboratory of Translational Cell and Tissue Research, Department of Pathology, UZ Leuven, Leuven, Belgium
[15]These authors contributed equally
[16]Senior author
[17]Lead Contact
*Correspondence: jeanchristophe.marine@kuleuven.vib.be
https://doi.org/10.1016/j.cell.2018.06.025

SUMMARY

Many patients with advanced cancers achieve dramatic responses to a panoply of therapeutics yet retain minimal residual disease (MRD), which ultimately results in relapse. To gain insights into the biology of MRD, we applied single-cell RNA sequencing to malignant cells isolated from BRAF mutant patient-derived xenograft melanoma cohorts exposed to concurrent RAF/MEK-inhibition. We identified distinct drug-tolerant transcriptional states, varying combinations of which co-occurred within MRDs from PDXs and biopsies of patients on treatment. One of these exhibited a neural crest stem cell (NCSC) transcriptional program largely driven by the nuclear receptor RXRG. An RXR antagonist mitigated accumulation of NCSCs in MRD and delayed the development of resistance. These data identify NCSCs as key drivers of resistance and illustrate the therapeutic potential of MRD-directed therapy. They also highlight how gene regulatory network architecture reprogramming may be therapeutically exploited to limit cellular heterogeneity, a key driver of disease progression and therapy resistance.

INTRODUCTION

Acquisition by cancer cells of a plethora of resistance-conferring genetic alterations greatly limits the clinical utility of most anti-cancer drugs. Therefore, there is a need to improve the effectiveness of treatment before mutational-acquired resistance prevails. Relapse is driven by a small subpopulation of residual or "drug-tolerant" cells, which are traditionally called "minimal residual disease" (MRD), that remain viable upon drug exposure, whereas the rest of the cell population is rapidly killed. Recent *in vitro* findings have indicated that the emergence of these persisters is unlikely due to mutational mechanisms (Menon et al., 2015; Sharma et al., 2010). Instead, drug tolerance is thought to be caused by the enrichment of a small subpopulation of cancer (stem) cells that is intrinsically refractory to the effects of anti-cancer drugs (Roesch et al., 2013; Trumpp and Wiestler, 2008). A non-mutually exclusive scenario proposes that the drug-tolerant phenotype is transiently acquired by a small proportion of cancer cells through non-mutational mechanisms (Menon et al., 2015; Sharma et al., 2010; Su et al., 2017)

Identification, characterization, and targeting of MRD are likely to improve outcomes and may even lead to cure (Luskin et al., 2018). Unfortunately, due to major clinical and technical challenges to sampling, much of what we know to date about MRD's biology of solid cancers comes from *in vitro* studies and, in particular, from investigations of the adaptive response of cultured BRAF mutant melanoma cells to selective $BRAF^{V600E/K}$

Please cite this article in press as: Rambow et al., Toward Minimal Residual Disease-Directed Therapy in Melanoma, Cell (2018), https://doi.org/10.1016/j.cell.2018.06.025

and MEK-inhibitors. One such study showed that uniform upregulation of the melanoma survival oncogene MITF drives an early non-mutational drug tolerance state and that pharmacological suppression of MITF-sensitized melanoma cells to MAPK-pathway inhibition (Smith et al., 2016). Consistently, enhanced MITF expression has been linked to innate/intrinsic resistance (Gopal et al., 2014; Haq et al., 2013a, 2013b; Ji et al., 2015; Johannessen et al., 2013; Müller et al., 2014; Smith et al., 2013; Van Allen et al., 2014; Wellbrock and Arozarena, 2015).

In apparent contrast, overwhelming evidence indicates that melanoma cells with a mesenchymal-like or a so-called "invasive" gene expression signature, characterized by low levels of MITF and SOX10 and high levels of AXL, are also intrinsically resistant to MAPK-inhibition (Kemper et al., 2014; Konieczkowski et al., 2014; Müller et al., 2014; Shaffer et al., 2017; Titz et al., 2016; Verfaillie et al., 2015). Drug-induced phenotype switching from a "proliferative" to an "invasive" state was therefore proposed as an alternative route toward drug tolerance and/or resistance (Kemper et al., 2014). More recently, adaptive resistance to RAF inhibition was shown to be driven by yet another melanoma subpopulation of slowly dividing cells that express low levels of MITF and high levels of NGFR (Fallahi-Sichani et al., 2017; Su et al., 2017).

Whether these distinct $MITF^{high}$ and/or $MITF^{low}$ transcriptional states contribute to drug tolerance *in vivo* and, if so, whether they co-occur within the same lesion is unknown. This is a highly clinically relevant question. Indeed, if distinct subpopulations of drug-tolerant cells can co-emerge within the same MRD, probing the magnitude of cellular heterogeneity and understanding the molecular mechanisms underlying the selection of drug-tolerant subpopulations will be essential to inform the rational selection of a second- or a third-line therapy.

Here, we sought to study the biology of solid tumor MRD in a clinically relevant *in vivo* context. We chose MAPK-targeted therapy of BRAF mutant melanoma as a paradigm. We developed patient-derived xenograft (PDX) models, allowing tracking and isolation of single residual cancer cells and leveraged the power of single-cell transcriptomics to gain insights into drug tolerance dynamics and heterogeneity.

RESULTS

Modeling MRD *In Vivo*

We established PDXs (i.e., MEL006, MEL015, and MEL007) from $BRAF^{V600E/K}$ mutant melanoma patients who experienced progressive disease and eventually showed marked sensitivity to a $BRAF^{V600E/K}$ inhibitor (i.e., dabrafenib) used either alone or in combination with a MEK (i.e., trametinib) inhibitor (Figure S1A). Before establishing the MEL006 cohorts, we dissociated melanoma lesions, and single-cell suspensions were transduced with dsRed-encoding lentiviruses (Figure 1A). Once tumors reached a comparable size, mice were exposed to the dabrafenib-trametinib (DT) combination (Figure 1B). All treated lesions rapidly shrunk (phase 1) to reach an impalpable size (phase 2) within 15 days. Continuous treatment invariably led to development of resistance (phase 3), indicating the presence of MRD. Although time to resistance substantially varied from mouse to mouse, comparable response rates and median survivals in repeated trials were seen at the population level (Figure S1B). We observed similar drug response profiles in the other two PDX models (Figure S1B; data not shown).

Consistent with mutational events being a key driver of acquired resistance, targeted DNA sequencing identified *de novo* mutations in the *MEK1* and *NRAS* genes and *BRAF* amplification in several lesions that acquired the ability to regrow ON treatment (Figure S1C). An alternative splicing event at the *BRAF* locus was also identified in one of these samples. All these events had previously been identified in patients with acquired resistance to MAPK-inhibitors (Rizos et al., 2014; Long et al., 2014).

To establish the genomic clonal architecture at the single-cell level (Macaulay et al., 2016), we isolated MEL006 dsRed-positive cells from drug-naive (T0) and MRD (phase 2) and subjected the genomic DNA of individual cells to massively parallel sequencing (Figure S1D). As expected, the CN profiles were complex, with clear heterogeneous alterations in chromosomes 2 and 7. This diversity enabled the inference of distinct subpopulations through hierarchical clustering. Critically, the subclonal distribution at T0 and MRD did not differ significantly. Analysis of a larger number of cells by DNA fluorescence *in situ* hybridization analysis confirmed this finding (Figure S1E). These data indicated that MRD is established through a non-mutational adaptive process and that PDXs are well-suited for studying the mechanisms of drug tolerance *in vivo*.

MRD Comprises both MITF-High and MITF-Low Melanoma Cells

Bulk RNA sequencing (RNA-seq) indicated that the intensity of the overlapping pigmentation/differentiation and MITF-driven gene expression signatures peaked at MRD (phase 2; Figure 1C). In contrast, both Hoek's and Verfaillie's invasive gene expression signatures decreased upon drug exposure (Figure 1C).

MITF immunostaining was rather uniform in drug-naive lesions with most cells exhibiting both diffuse cytoplasmic and nuclear positivity. Consistent with the increase in MITF activity upon MAPK-inhibition, marked nuclear staining was seen in a fraction of the melanoma cells at phase 2 (Figure 1D). An increase in pigmentation, which is a likely consequence of increased MITF activity, was also seen in a small proportion of the drug-tolerant melanoma cells (Figure 1D). Critically, there was also a large fraction of cells that became completely devoid of any MITF staining at phase 2 (Figure 1D). Similar results were obtained with the MEL015 and MEL007 PDX models (data not shown). These data indicated that the adaptive response to MAPK-inhibition is not uniform. Instead, distinct subpopulations that exhibit very different levels of MITF can emerge *in vivo* within a single MRD lesion.

Single-Cell RNA-Seq Identifies Distinct Drug-Tolerant States

To probe the extent of transcriptional state diversity and portray the dynamics of cell-state transition during drug response, we measured a thousand transcriptomes from individual melanoma cells isolated at different time points. The single-cell RNA-seq (scRNA-seq) data, which were processed using a pipeline that was conceptually similar to PAGODA (Fan et al., 2016),

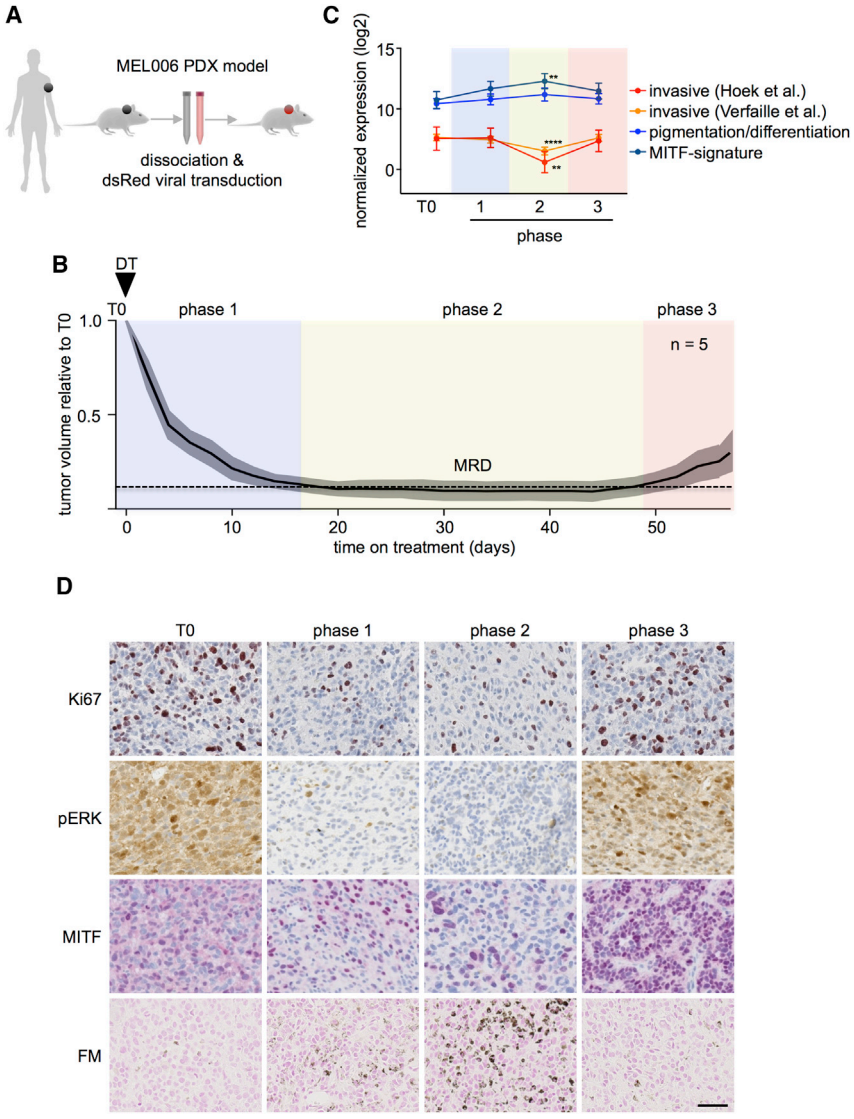

Figure 1. MRD Exhibits MITF High and Low Drug-Tolerant Cells

(A) Establishment of PDX model MEL006 to study MRD composition in an *in vivo* preclinical context.

(B) Mean tumor volumes (±SEM) relative to baseline (T0) for five representative MEL006 mice treated with dabrafenib-trametinib (DT).

(C) Dynamics of known gene expression signatures during BRAF/MEK inhibition based on bulk RNA-seq. Error bars represent 95% confidence intervals of different genes among gene expression signatures (n = 3 biological replicates), **p < 0.001; ****p < 0.0001; Mann-Whitney test.

(D) Immunostainings for Ki67, pERK, MITF, and pigment (Fontana-Masson silver method) at the different drug-response phases highlighted in (B). Scale bar represents 50 μm.

See also Figure S1.

confirmed the emergence of cells exhibiting contrasting levels of MITF activity at phase 2 (Figure 2A).

Four distinct melanoma transcriptional states were detected at this time point (Figures 2B and 2C). One cluster overlapped with the subpopulation of cells exhibiting very high MITF activity and expressed markers of differentiation and pigmentation, such as TRPM1, GPR143, and MLPH (Figures 2D and 2E). This "pigmented" subpopulation was enriched at phase 1-2 (Figure 2C).

One subpopulation associated with expression of markers of an epithelial-to-mesenchymal (EMT) signature and the "invasive" melanoma state (Hoek et al., 2008; Verfaillie et al., 2015), such as SLIT2, BGN or TNC (Figures 2D and 2E). These cells exhibited low levels of MITF (Figure 2A). Unexpectedly, their percentage dropped progressively from T0 to phases 1 and 2, indicating that drug tolerance is not driven by a proliferative to invasive phenotype switch in this particular model (MEL006).

Another cluster was characterized by high expression of neural crest stem cell (NCSC) markers, including NGFR, AQP1, or GFRA2 (Figures 2D and 2E). Similarly to "invasive" cells, NCSCs exhibited very low to undetectable MITF activity (Figure 2A). In contrast to the invasive cells, however, these cells sustained high levels of expression and transcriptional activity of the neural crest specifier SOX10 (Figure S2A) and their proportion increased upon drug exposure (Figure 2C).

Most remaining cells at phase 2 exhibited intermediate MITF activity (Figures 2A and 2B), and expressed high levels of CD36, SLC7A8, SLC12A7, or DLX5 (Figure 2D). These cells also expressed a set of genes upregulated in nutrient-deprived cells (Figure 2E), on the basis of which we named them "starved"-like melanoma cells (SMCs). Critically, SMCs were particularly enriched at phase 1 and, to a lesser extent, phase 2 (Figure 2C).

Note that the SMCs were clearly distinct from other MITF intermediate cells, which expressed the classical "proliferative" gene signature and were all detected at T0 and resistant (phase 3) lesions (Figures 2A, S2B, and S2C). As expected, these "proliferative" melanoma cells expressed genes associated with a recently described cancer cell metabolism signature (Figure S2D) (Kim et al., 2016). In contrast, expression of these metabolic genes was drastically decreased in all drug-tolerant subpopulations, including the SMCs (Figure S2D).

We reconstructed the transcriptional dynamic time course and lineage relationships using Monocle (Trapnell et al., 2014). The cells were distributed along pseudo-temporally ordering paths from "proliferative" melanoma cells to MITF^{high} "pigmented" cells (differentiation lineage) or to MITF$^{low/negative}$ cells, which either adopted the SOX10^{low} "invasive" or SOX10^{high} NCSC

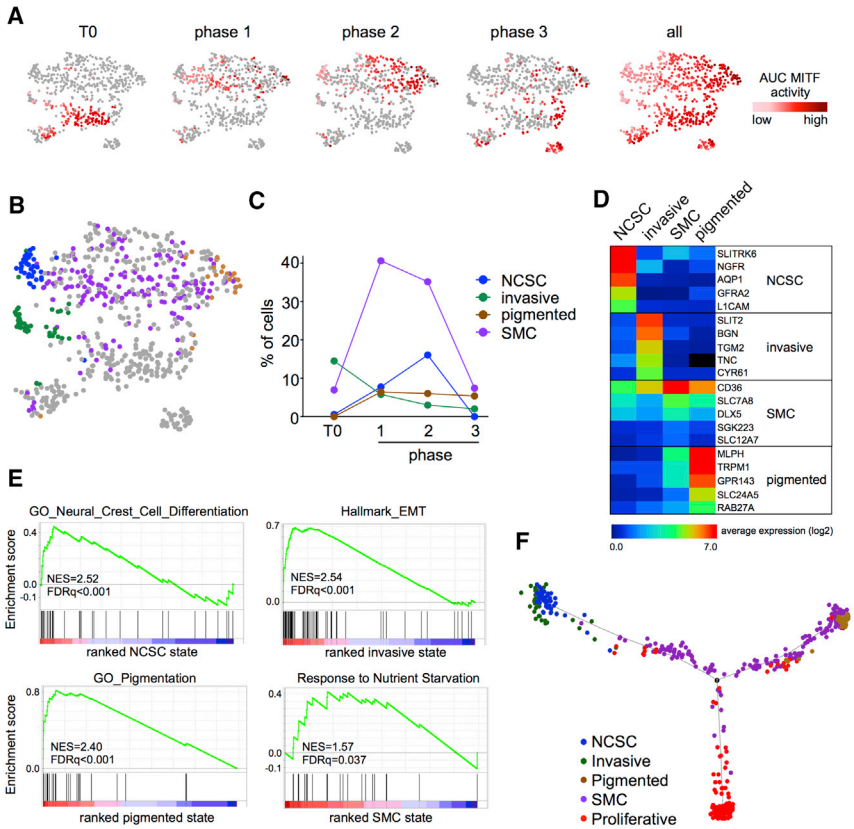

Figure 2. scRNA-Seq Identifies Multiple Co-existing Drug-Tolerant Transcriptional States

(A) Shown are T-distributed stochastic neighbor embedding (t-SNE) plots of the different treatment phases colored based on the expressional activity of the MITF state.

(B) Single-cell transcriptomics allow the identification of four different drug tolerant cell states. Shown is the projection of 674 cells in a two-dimensional space by t-SNE. The cell-state identity was inferred by enrichment analysis. Cells in a higher state were colored using AUCell analysis.

(C) Dynamics of the different cellular states at the indicated time points.

(D) Heatmap shows representative genes (population averages) for NCSC, invasive, SMC, and pigmented cellular states.

(E) Gene set enrichment analysis (GSEA) shows enrichment of gene sets related to neural crest differentiation, response to nutrient starvation, EMT, and pigmentation across the different drug tolerant single-cell states. NES, normalized enrichment score; FDR, false discovery rate.

(F) Monocle-based pseudo-time ordering predicts that drug-exposed melanoma cells move along two different trajectories (differentiation and dedifferentiation).

See also Figure S2 and Table S1.

states (dedifferentiation lineage). The SMCs followed the "proliferative" cells and were present at the branching point, thus preceding both end states. This particular cell ordering was further supported by Destiny-based diffusion plots (Angerer et al., 2016) (Figure S2E). These data suggest that drug exposure first promotes a transient transition from a "proliferative" to a "starved"-like state from which cells then make the decision to move along a differentiation trajectory to become "pigmented" or a dedifferentiation path and to either become NCSCs or invasive. In the case of MEL006, cells favored entry into the NCSC over the invasive state.

None of the drug-tolerant states exhibited mitotic activity (data not shown), indicating that acquisition of drug-tolerance may require cells to exit the cell cycle. Notably, both NCSC and SMC subpopulations had drastically decreased in drug-resistant tumors (phase 3; Figure 2C). This observation raised the possibility that these cells either do not directly contribute to resistance or can only do so following transcriptional reprogramming.

MRD Shows Geographic Heterogeneity

To obtain information about the spatial distribution of the various drug-tolerant states we performed immunostaining for the most discriminative markers of the NCSC (i.e., AQP1), SMC (i.e., CD36), pigmented (MLANA, also known as MART-1) and invasive (i.e., AXL) subpopulations. Single-marker staining confirmed the dramatic increase in the intensity of expression and the number of AQP1+, MLANA+, and CD36+ (but not AXL+) cells in MEL006 MRD (Figures 3A, 3B, and S3A–S3C).

Only rare AQP1 cells were detected at T0 and in drug-resistant lesions. Note that AQP1 is also expressed in endothelial cells. Co-staining further confirmed that most AQP1-positive detected in MRD were of melanoma origin, as illustrated by their positivity for the marker S100, and that AQP1 and MITF were anti-correlated in these cells (Figures 3C, 3D, and S3B). In contrast, CD36- and MLANA-positive cells showed high and very high nuclear MITF immunoreactivity, respectively (Figure 3C).

Most AQP1-positive melanoma cells also expressed SOX10 and NGFR at phase 2, but not the invasive marker AXL (Figure S3B). Whereas a fraction (10% to 15%) of melanoma cells was strongly positive for AXL at T0, their occurrence was rarer (<5%) at phase 2. None of the AQP1+ cells expressed the proliferation marker Ki67 (Figure S3B).

We used multiplexed immunohistochemistry (IHC) (Tsujikawa et al., 2017) to further visualize the relative spatial distribution of the various drug-tolerant subpopulations (Figure 3E). This analysis confirmed that the selected panel of markers was sufficient to discriminate between the various, non-overlapping drug-tolerant states. This also confirmed their increased abundance in MRD compared to T0 (Figure S3C). To enable quantitative localization of cellular phenotype we utilized a multiparameter cytometric quantification approach via evaluation of chromogenic intensities using single-cell segmentation algorithms

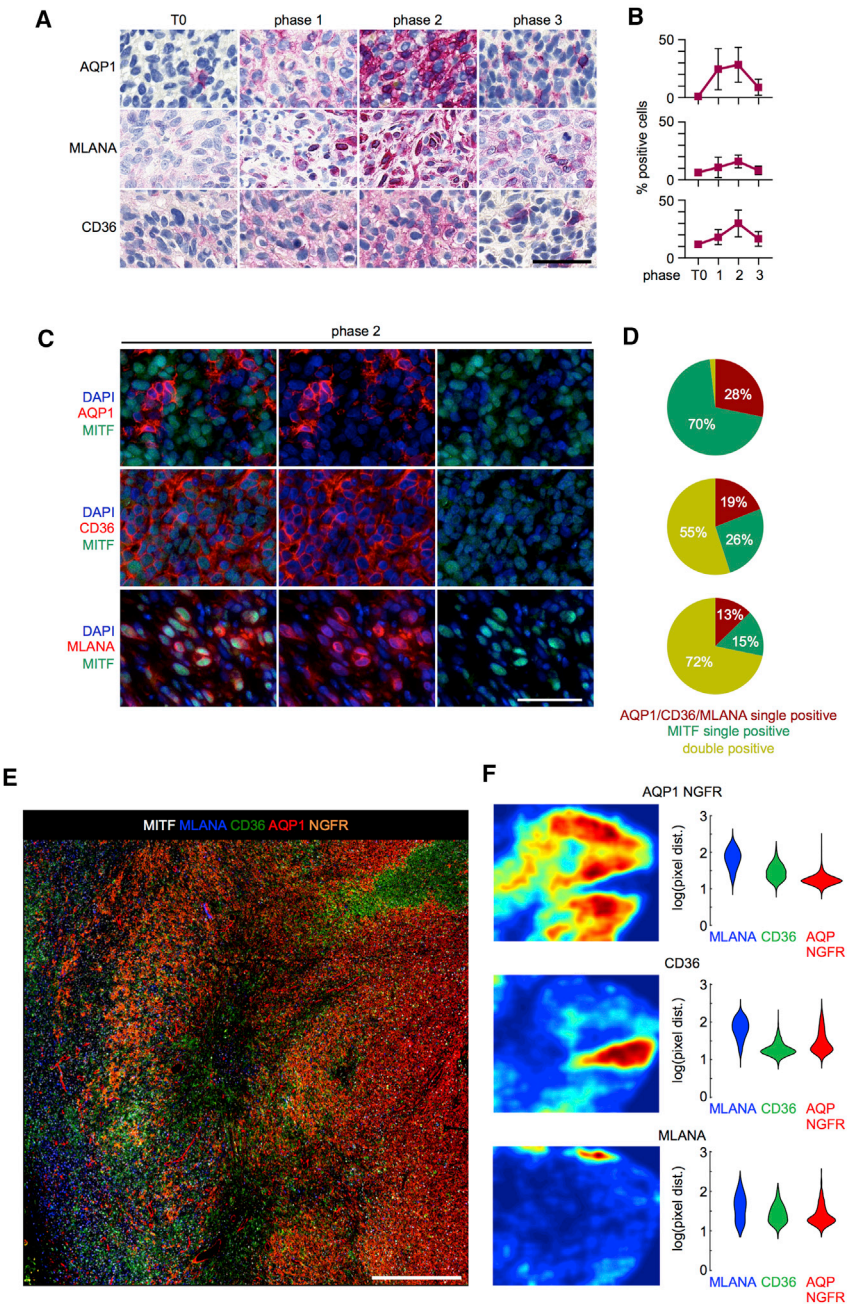

Figure 3. MRD Exhibits Geographic Heterogeneity

(A) Expression of AQP1, MLANA and CD36 before and at the different phases during treatment with BRAF/MEK inhibition. Scale bar, 50 μm.

(B) Quantification of the immunostainings presented in (A). Percentage of AQP1-, MLANA-, and CD36-positive cells are shown for the indicated time points. Fifteen high-power fields were counted for AQP1 (due to the geographic variability) and five high-power fields for MLANA and CD36 from 3 replicates. Data are presented as mean ± standard deviations (SD).

(C) Double staining for MITF (green) and AQP1, CD36, or MLANA (red). Scale bar, 50 μm.

(D) Quantification of data presented in (C). Five high-power fields from 3 replicates were counted to represent the mean percentages of AQP1/CD36/MLANA single-positive (red), MITF single-positive (green), and double-positive cells (yellow). Double-negative cells (DAPI only) were not taken into account.

(E) Multiplex immunostaining for MITF (white), MLANA (blue), CD36 (green), AQP1 (red), and NGFR (orange). Scale bar, 600 μm.

(F) Heatmap showing the intensity of AQP1/NGFR-, CD36-, and MLANA-positive cells (left) and violin plots highlighting the spatial organization of each cells population relative to other populations as defined by their respective markers (right); pixel dist. = pixel distance between the center position of two cells.

See also Figure S3.

(Tsujikawa et al., 2017). Thresholds or gates were set for quantification of single-cell based intensity information for each marker and verified by visual confirmation of cell position on the original stain. Using a sequential gating strategy, we identified MLANA+CD36− (pigmented), CD36+MLANA− (SMC), and CD36-MLANA-AQP1+NGFR+ (NCSC) cells (Figure S3D), all of which were AXL-. Co-staining of both AQP1 and NGFR was required to distinguish the NCSC state from AQP1+ endothelial cells. Importantly, proportional analysis of each cell state confirmed a predominance of AQP1+NGFR+ cells on treatment and that MITF expression is highest in MLANA+, intermediate in CD36+, and absent in AQP1+NGFR+ cells (Figures 3E and S3D).

Density plots, which show the distribution of the different discriminative markers, revealed specific spatial patterns for the various cell states (Figure 3F). Using positional information acquired from the single-cell segmentation we generated violin plots that display the shortest distance between each individual cell to cells of the same state or cells of other states. This analysis revealed that the NCSC subpopulation occurred in clusters (closer to each other than to other states); as did the CD36-positive SMCs. MLANA^{+} cells were closer to the NGFR/AQP1-double positive cells than they were to each other, indicating dispersion of these cells within the NCSC clusters. Melanoma MRD thus exhibits geographic heterogeneity governed by the clustering of drug-tolerant subpopulations.

MRD Composition Exhibits Marked Interpatient Variability

To infer the composition of MRD from very small amounts of input material, we compare mRNA levels of the 6 most discriminative markers for each drug-tolerant state between the

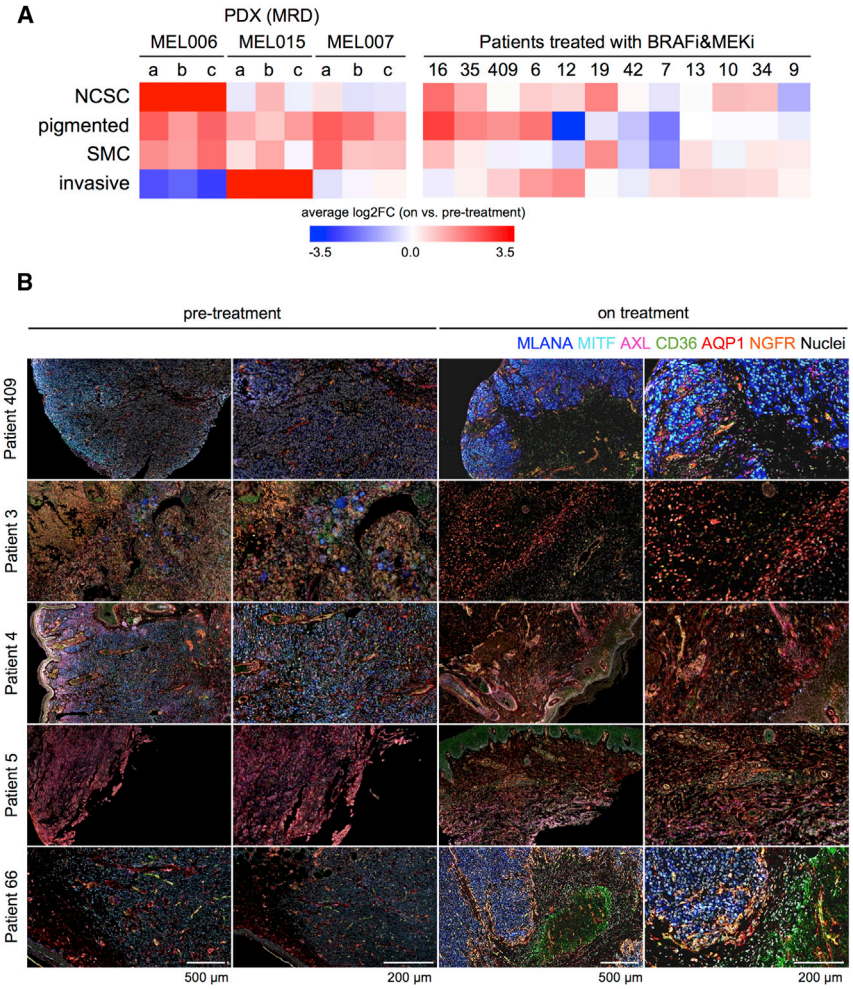

Figure 4. MRD Composition Exhibits Marked Interpatient Variability

(A) Estimation of drug-tolerant state activity in bulk samples by either qRT-PCR (PDX samples) or bulk RNA-seq (human patients). ON-treatment samples were compared to matched before-treatment samples (fold change).

(B) Sequential chromogenic IHC on (sub)cutaneous metastases from patients treated with the BRAF/MEK combination: pre-treatment (left) and during treatment (right). The color of each of the markers is indicated.

See also Figure S4.

treated lesion and its matched drug-naive counterpart, log2 transform and average. In concordance with the sc-RNA-seq and mIHC data, a reproducible increase in the NCSC, SMC and pigmented, but not invasive, subpopulations was detected in MEL006 MRD (Figure 4A). A similar analysis predicted a predominant increase in the invasive and pigmented or SMC and pigmented subpopulations in MEL015 and MEL007 MRDs, respectively (Figure 4A). Importantly, these predictions were confirmed by mIHC analyses (Figures S4A–S4C). Note that in contrast to the NCSC and CD36+ cells, AXL-positive cells did not occur in clusters, but presented a rather dispersed pattern (Figure S4D). Together, these data indicated that MRD composition can vary substantially between different PDX models.

To assess the clinical relevance of these findings, we isolated paired tumor materials from drug-naive and biopsy specimens of patients exposed to BRAF/MEK therapy and performed bulk RNA-seq. Strikingly, co-emergence of NCSC, MCS, invasive, and/or pigmented subpopulations was detected in most "drug-exposed" biopsies (Figure 4A). We also observed marked inter-patient variability. These findings were further validated by mIHC (Figures 4B and S4E). Representative images from 5 patient biopsies pre- and on treatment are shown. These images were selected to illustrate the co-occurrence of several drug-tolerant states and the marked interpatient variability. Adaptive tolerance to MAPK-inhibition thus leads to the co-occurrence of (varying combinations of) up to four distinct transcriptional states (i.e., pigmented, SMC, NCSC, and invasive states) within a single MRD.

NCSCs Emerge in MRD through Cell-State Transition

One of the predominant drug-tolerant states in ON-treatment patient biopsies was the NCSC state. Interestingly, the NCSC marker NGFR has been associated with stem-like properties (Fallahi-Sichani et al., 2017; Menon et al., 2015; Redmer et al., 2014; Shaffer et al., 2017). Consistently, GSEA identified significant similarities between the NCSC signature and quiescent neural stem cell profiles (Codega et al., 2014; Llorens-Bobadilla et al., 2015), as well as with other cancer stem cell profiles (Figures 5A, S5A, and S5B). There was also an overlap with a signature from the therapy-resistant glioblastoma proneural subtype (Verhaak et al., 2010) and the drug-persister signature from a lung cancer cell line (Figures 5A, S5A, and S5B) (Sharma et al., 2010). These data indicated that the NCSC subpopulation may exhibit stem cell-like properties and, as such, may play a prominent role in driving relapse.

To search for NCSCs in a large cohort of human clinical samples we inspected The Cancer Genome Atlas (TCGA) bulk RNA-seq dataset (n = 469). AQP1 and GFRA2 expression was detected in a small subset (<7%) of skin cutaneous melanomas (SKCM; n = 32; Figures S5C and S5D). Strikingly, expression of most NCSC markers was elevated in all GFRA2^{high} compared to GFRA2^{low} samples and vice versa. In contrast, MITF levels were lower in the GFRA2^{high} samples. Thirty-one out of the 32 GFRA2^{high} samples were obtained from drug-naive patients, indicating that NCSCs are present in non-negligible amounts in a fraction of untreated melanoma

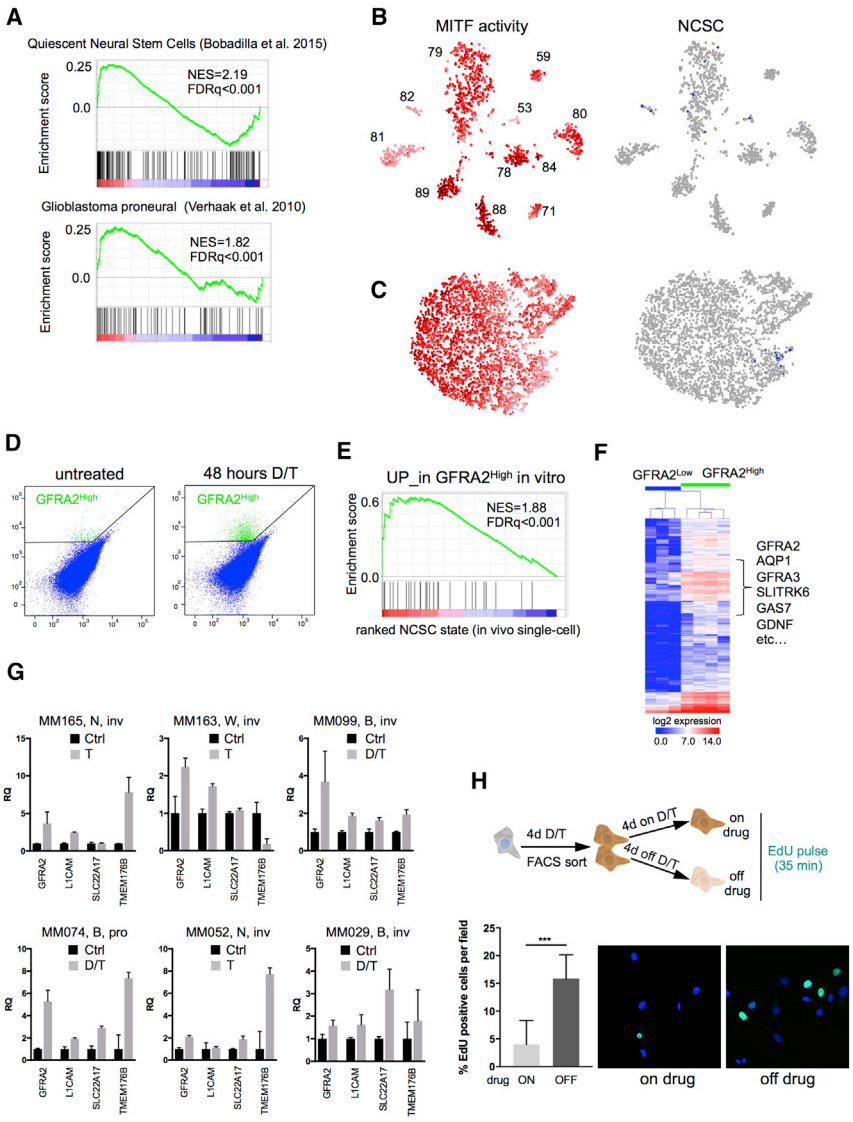

Figure 5. NCSCs Emerge in MRD through Cell-State Transition

(A) GSEA shows enrichment of gene sets related to quiescent neural stem cells and pro-neural glioblastoma across the melanoma NCSC state. NES, normalized enrichment score; FDR, false discovery rate.

(B) Detection of rare (MITF^{low}) NCSCs in treatment naive human melanomas (blue cells) by scRNA-seq (Tirosh et al., 2016).

(C) Detection of rare (MITF^{low}) NCSCs in treatment naive PDX (MEL006) samples (blue cells) by scRNA-seq (10× genomics).

(D) Representative FACS profiles of GFRA2 expression. GFRA2 expression is induced in MEL006 cells upon treatment with combined BRAF/MEK inhibition.

(E) GSEA plot shows significant enrichment for the top-100 upregulated genes in FACS-sorted GFRA2^{high} cells across *in vivo* single-cell NCSC states.

(F) Heatmap shows gene expression profile (RNA-seq) of FACS-sorted GFRA2^{high} versus GFRA2^{low} cells after ten days of treatment. Additional NCSC markers are co-expressed with GFRA2.

(G) Treatment induced upregulation of GFRA2 expression and other NCSC markers in different melanoma short-term cultures (qRT-PCR; pro, proliferative; inv, invasive molecular phenotype). Error bars represent SD of 3 biological replicates.

(H) Drug washout experiments show the reversibility of the NCSC state to re-entering into the cell cycle as assessed by EdU pulse experiments. Error bars represent SD confidence intervals of 10 images from three biological replicates. ***p = 0.001; Mann-Whitney test.

See also Figure S5.

lesions. Importantly, there was no significant association between the presence of these cells and the *BRAF*, *NRAS*, or *NF1* mutational status.

Inspection of publicly available single-cell data (Tirosh et al., 2016) further established the presence of NCSCs (20 of 1,252 melanoma cells), which all exhibited low MITF activity, in various drug-naive metastatic lesions from 4 of 11 patients (Figure 5B). Our own single-cell data indicated that the NCSC population was present in minute amount (0.58%; 1 of 172 cells) in drug-naive MEL006 lesions. This was further validated by scRNA-seq of a larger number (>4,000) of T0 melanoma cells (Figure 5C). Only 24 of 4,352 (0.55%) cells sequenced exhibited the characteristic NCSC transcriptome. The proportion of NCSC increased by 13-fold (7.74%) at phase 1, a time point at which the lesion had only decreased by 50% of its initial volume (Figure 2C). Given that cell proliferation drops abruptly during this first drug response phase, emergence of such a high number of NCSCs at phase 1 cannot solely be due to the selection of a rare pre-existing NCSC subpopulation. In contrast, the data established that therapeutically challenged melanoma cells transit into the NCSC state through transcriptional reprogramming.

Transition into the NCSC State Is Cell Autonomous and Reversible

To assess whether emergence of NCSCs upon MAPK inhibition is cancer cell intrinsic, we exposed 2D cultures of MEL006 to near IC_{25} concentrations of dabrafenib-trametinib for 10 days. Fluorescence-activated cell sorting (FACS) analysis revealed a 10-fold increase in GFRA2-positive cells in dabrafenib-trametinib-exposed cultures (Figure 5D), but not in cells exposed to other cell proliferation inhibitors such as CDK4/6 or mTOR-inhibitors (data not shown). Bulk transcriptome analysis of FACS-sorted GFRA2^{high} cells revealed a striking increase in expression of NCSC markers as compared to the GFRA2^{low} subpopulation, and GSEA established a significant overlap between the transcriptome of these *in-vitro*-cultured cells and the NCSCs

isolated from PDXs' MRD (Figures 5E and 5F). Moreover, single-cell transcriptome analysis of the FACS-sorted GFRA2^{high} population further confirmed the enrichment in cells harboring the NCSC gene signature (Figure S5E). These data indicated that *in vitro* cultures of MEL006 exposed to MAPK-inhibitors do produce NCSCs.

To further investigate the generality of this effect, and in particular whether emergence of the NCSCs dependents on the genetic background, we exposed a series of short-term melanoma cultures to concurrent BRAF and/or MEK-inhibition (Figures 5G and S5F). Critically, upregulation of NCSC markers was observed in all BRAF mutant cultures, whether they exhibited a "proliferative" (i.e., MM074) or an "invasive" profile (i.e., MM029 and MM099). A similar increase was observed in NRAS mutant (i.e., MM052 and MM165) and triple wild-type (i.e., MM163) cultures upon exposure to trametinib (T). Because expression of the NCSC markers was undetectable in some of these cultures (i.e., MM029), these data further supported the possibility that melanoma cells can transit into the NCSC state through phenotype switching, and thus regardless of their initial transcriptional state and driver mutations.

To determine whether the NCSC state is reversible, we exposed MEL006 cells to sub-lethal doses of dabrafenib-trametinib for 4 days and subsequently cultured the cells in presence or absence of drugs (Figure S5G). Whereas an upregulation of NCSC markers was observed in drug-exposed cultures, a progressive decrease in expression of these markers was observed following drug removal. In a separate experiment, MEL006 cells were pre-treated for 4 days with dabrafenib-trametinib before GFRA2^{high} cells were isolated by FACS and allowed to grow for another 4 days in presence or absence of drugs. An EdU-incorporation assay was then performed (Figure 5H). Whereas GFRA2^{high} cells remained quiescent under therapeutic pressure, they acquired the ability to proliferate upon drug removal. In keeping, a progressive decrease in the proportion of GFRA2^{high}-cells was observed in a FACS-enriched population of GFRA2^{high} cells from the MM052 short-term culture grown in drug-free medium (Figure S5H). Note that, as expected, GFRA2^{high}-cells were significantly less sensitive to dabrafenib-trametinib than GFRA2^{low} cells (Figure S5I). These data demonstrated that MAPK-inhibition induces a quiescent NCSC state, which is transient and reversible. The kinetics of the inter-conversion between GFRA2-high and GFRA2-low cells in culture further supports a model in which transition in and out of the NCSC state is driven by a non-mutational, adaptive reprogramming process. Importantly, NCSCs have the capacity to re-enter the cell cycle and give rise to proliferating (GFRA2-negative) progenies.

RXR Signaling Is a Key Driver of the NCSC State

SCENIC is a robust clustering method for the identification of stable cell states from scRNA-seq data based on the underlying gene regulatory networks (GRNs) (Aibar et al., 2017). This method confirmed the clear distinction between the pigmentation, NCSC, "invasive," "proliferative" and SMC states and identified their underlying regulons (Figures 6A, 6B, S6A, and S6B).

SCENIC predicted a complex regulatory network underlying the NCSC state that is partly driven by SOX transcription factors (TFs), MEF2C and TFAP2B (Figure 6B). Consistently, SOX10 levels and activity are high in the NCSCs (Figure S2A). Interestingly, MEF2C is a direct transcriptional target of SOX10 (Agarwal et al., 2011). Moreover, SOX10 and MEF2C physically interact and function cooperatively to activate the MEF2C gene in a feed-forward transcriptional circuit. Interestingly, MEF2C was recently identified as an effector of neural crest development (Hu et al., 2015). Similarly, TFAP2B (or AP-2β) is also required for the development of the neural crest and its derivatives (Martino et al., 2016). Another component of this GRN is the retinoid X receptor-γ (RXRG; Figure 6B). IHC confirmed that the majority of AQP1+ cells present in MRD express high nuclear levels of SOX10, MEF2C, TFAP2B, and RXRG (Figures 6C and S6C).

Inspection of the GRN highlighted a putative prominent role for RXRG in this network as most of the discriminative NCSC markers, including GFRA2, GFRA3, AQP1, NGFR, and, even, SOX10 were predicted to be direct target of this TF (Figure 6D). RXR functions primarily by heterodimerizing with and regulating the activity of a dozen of nuclear receptors (Evans and Mangelsdorf, 2014). In "permissive" heterodimers, such as RXR/PPAR and RXR/LXR, ligand activation of RXR results in transcriptional activation. Certain natural lipids, such as 9-*cis* retinoic acid, and synthetic compounds, such as bexarotene (B), selectively and potently activate such transcriptional response. Interestingly, an increase in the proportion of GFRA2-positive cells was observed upon exposure of MEL006 cultures to bexarotene either alone, or in addition with dabrafenib-trametinib (Figure 7A). An increase in GFRA2 levels was observed in *NRAS* mutant and triple wild-type melanoma cultures exposed to both trametinib and bexarotene (Figures 7B and 7C). These data indicated that liganded RXR can induce a transcriptional switch toward the NCSC state, and thus regardless of the genetic background and initial transcriptional state. Conversely, pharmacological inhibition of RXR by HX531 (HX), a potent and selective RXR antagonist (Ebisawa et al., 1999), inhibited the drug-dependent emergence of GFRA2-positive cells (Figures 7A and S7A). Together, these data established RXR signaling as a key driver of the NCSC state.

Targeting RXR Signaling Delays Time-to-Disease Progression

The possibility to pharmacologically modulate the abundance of the NCSC subpopulation offered the opportunity to test its putative contribution to drug resistance. We used a short-term melanoma culture (MM52) that exhibits a robust increase in NCSCs in response to MAPK-inhibition (i.e., trametinib, or T). Treatment of these cells with HX or bexarotene alone did not induce measurable long-term growth effects. Strikingly, while bexarotene decreased the potency of trametinib, HX-sensitized cells to long-term exposure to the MAPK inhibitor (Figures 7D and 7E).

Consistently, whereas HX increased the response rates of MEL006 PDXs to the dabrafenib-trametinib combination, bexarotene administration mitigated their anti-tumor activity (Figure 7F). To assess the impact of HX exposure on the MRD composition we performed qRT-PCR and IHC analyses on MRD materials from mice treated with dabrafenib-trametinib and dabrafenib-trametinib+HX. While, as expected, an increase in NCSC markers was observed in MRD isolated

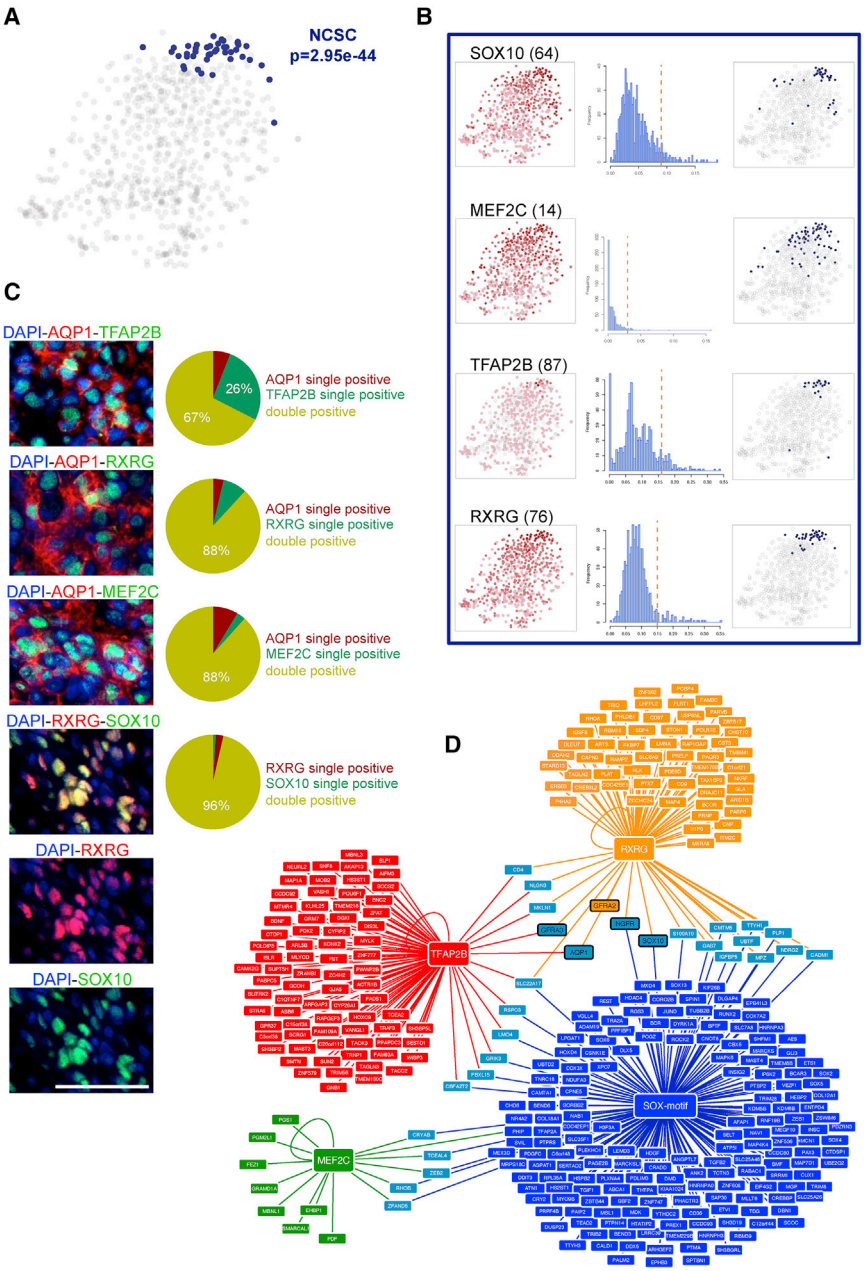

Figure 6. RXR Signaling Is a Key Driver of the NCSC State

(A) t-SNE shows cells colored by state identity (SCENIC approach). The identities are inferred by the binary activities of the TF regulons. Cell identities inferred by SCENIC are largely overlapping with the SCDE approach (***p hypergeometric distribution test).

(B) SCENIC analysis predicts TFs such as SOX10, MEF2C, TFAP2B, and RXRG as central hubs governing the NCSC state. TF regulon activities were quantified using AUCell.

(C) Left: immunostainings at phase 2 of MEL006 highlighting the expression of TFAP2B, RXRG, and MEF2C in AQP1-positive cells. RXRG and SOX10 colocalize. Scale bar, 50 μm. Right: quantifications of the immunostainings shown left with five high-power fields counted to represent the mean percentage of single-positive (red or green) and double-positive cells (yellow). Double-negative cells (DAPI only) were not taken into account.

(D) Gene regulatory network analysis using SCENIC identifies critical nodes driving the NDTC state. The predicted TFs and their target genes are shown.

See also Figure S6.

from mice treated with dabrafenib-trametinib, this was attenuated upon exposure to the triple combination (Figures S7B–S7D). Consistently, accumulation of AQP1+ cells in dabrafenib-trametinib+HX-treated mice was mitigated compared to mice challenged with dabrafenib-trametinib only. Importantly, concomitant to this drop, an increase in the other three drug-tolerant states, and in particular of the ''invasive'' state, was observed. IHC confirmed the dramatic upregulation of the ''invasive'' marker AXL in MRD from mice treated with the triple combination (Figures S7B and S7D).

Strikingly, combining HX with dabrafenib-trametinib produced a significantly longer median progression-free survival (PFS) period compared to the dabrafenib-trametinib treatment and delayed the development of resistance (50 days for dabrafenib-trametinib vs. 94 days for the triple combination; hazard ratio 0.23; 95% confidence interval [CI] 0.070–0.73; p = 0.0004). It is noteworthy that 20% of the PDXs treated with the dabrafenib-trametinib+HX combination never developed resistance under continuous treatment for up to 120 days (Figure 7G). This treatment did not cause any relevant adverse reaction or weight loss (data not shown).

DISCUSSION

Preventing disease relapse through the rational targeting of MRD is emerging as a putative salvage strategy for targeted and other cancer therapies (Luskin et al., 2018). We show herein that this approach is potentially more challenging than previously anticipated from bulk analyses and *in vitro* culture studies (Sharma et al., 2010; Smith et al., 2016). Using refined *in vivo* pre-clinical models of melanoma and patient biopsies, we indeed demonstrate that MRD is not uniform. Instead, MRD features both cellular and geographic heterogeneity.

We found that MRD from BRAF mutant melanoma lesions exposed to concurrent RAF/MEK-inhibition can contain up to 4 distinct drug-tolerant states. These findings illustrate the remarkable phenotypic plasticity of melanoma cells by their ability to escape the deleterious effect of this drug combination

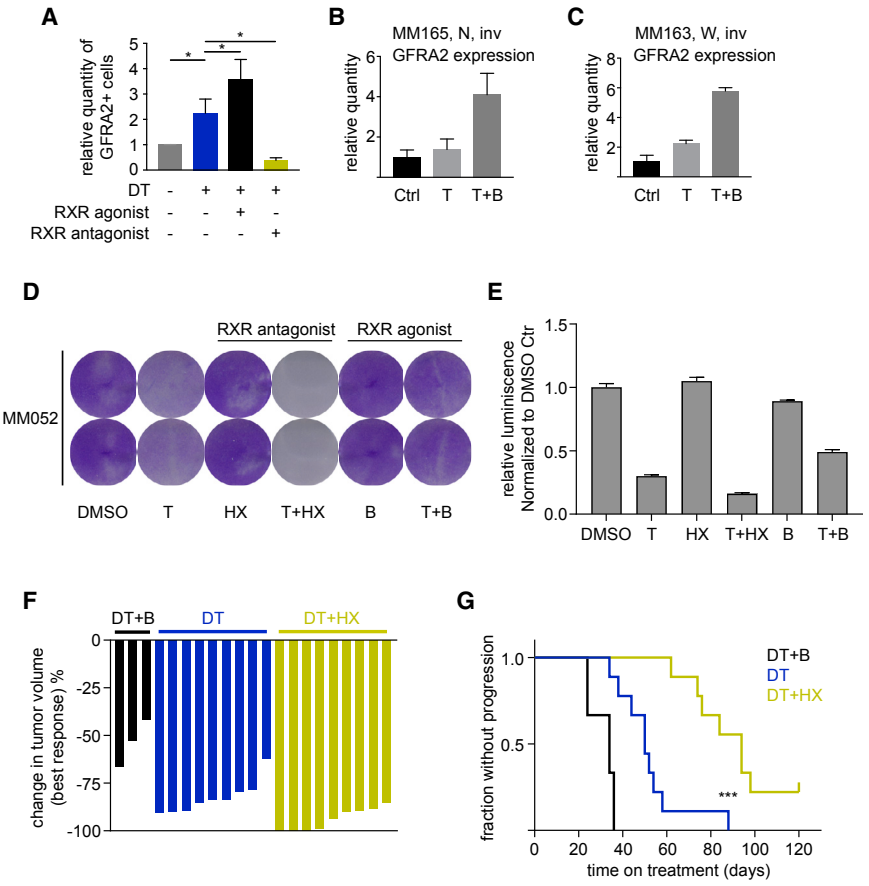

Figure 7. Targeting RXR Signaling Delays Time-to-Disease Progression

(A) Relative number of GFRA2+ cells are shown using FACS-sorting after treatment of MEL006 cells with either combined BRAF/MEK inhibition and/or RXR antagonist/agonist. Error bars represent SD of four biological replicates; *p < 0.05 Mann-Whitney test. DT, dabrafenib-trametinib; RXR agonist, bexarotene; RXR antagonist, HX531.

(B and C) Increase in GFRA2 expression (qRT-PCR) upon MEK inhibition (trametinib, T) and RXR agonist (bexarotene, B) treatment in *NRAS* mutant cells (MM165) (B) and wild-type cells (MM163) (C). Error bars represent SD of three biological replicates.

(D) Colony assay performed 7 days after incubating *NRAS* mutant short culture melanoma line MM052 with a MEK inhibitor (trametinib, T) and RXR antagonist (HX531, HX) or RXR agonist (bexarotene, B).

(E) A representative CellTiter-Glo assay performed 6 days after incubation of the short culture melanoma line MM052 with MEK inhibitor trametinib (T; 2 nM), RXR agonist bexarotene (B; 1 μM), and RXR antagonist HX531 (HX; 2 μM). Error bars represent variability from three technical replicates. Error bars represent SD.

(F) Waterfall plot showing best response (%) of MEL006 mice treated with dabrafenib-trametinib+B (n = 3), dabrafenib-trametinib alone (n = 9), and dabrafenib-trametinib+HX (n = 9). In the dabrafenib-trametinib+HX-treated group, three mice achieved a complete response.

(G) Kaplan-Meier curve for MEL006 mice treated with dabrafenib-trametinib+B (n = 3), dabrafenib-trametinib alone (n = 9), and dabrafenib-trametinib+HX531 (n = 9). Median time to progression was 34, 50, and 94 days, respectively. Log rank (Mantel-Cox) for dabrafenib-trametinib versus dabrafenib-trametinib+HX: p = 0.0004 (***) and hazard ratio (log rank): 0.23 (95% CI, 0.070 – 0.73).

See also Figure S7.

through very distinct mechanisms. One mechanism relies on the activation of a robust MITF transcriptional program, which triggers differentiation into highly pigment-producing cells. Another mechanism causes drug-exposed cells to turn on a "starvation"-like transcriptional program. Pseudo-time ordering methods predict that this is actually the first program that is engaged by the drug-naive, proliferating melanoma cells in response to drug exposure. Another, very distinct, mechanism of drug tolerance relies on the downregulation of MITF activity and induction of dedifferentiation toward either the invasive or the NCSC state. Importantly, although the NCSC and "invasive" states are both characterized by loss of MITF and differentiation markers, our scRNA-seq data provide unambiguous evidence that these transcriptional states represent two distinct subpopulations. The $MITF^{low}/SOX10^{low}/AXL^{high}$-invasive subpopulation has been extensively described (Hoek et al., 2006, 2008). These cells harbor a mesenchymal-like phenotype that is well known for its high intrinsic resistance to MAPK therapeutics in *in vitro* cultures (Konieczkowski et al., 2014; Müller et al., 2014; Shaffer et al., 2017; Verfaillie et al., 2015). An enrichment of this AXL^{high} subpopulation is a common feature of drug-resistant melanomas (Konieczkowski et al., 2014; Müller et al., 2014), and AXL-positive cells are rapidly selected upon therapeutic exposure (Boshuizen et al., 2018). In contrast to the invasive state, the NCSC state has so far only been poorly described.

While drug-resistance is often caused by acquisition of specific genetic alterations, we provide evidence that co-emergence of these distinct drug-tolerant states within MRD can be driven by adaptive, non-mutational, events. Moreover, in concordance with a recent study (Su et al., 2017), our data indicate that acquisition of, at least some, of these drug-tolerant states is the result of a "Lamarkian induction" (Huang, 2012; Pisco and Huang, 2015). We show that the dramatic enrichment of the NCSC subpopulation in MRD only can be due to *de novo* phenotypic transition toward this particular state through transcriptional reprogramming, as opposed to an enrichment of rare pre-existing cells.

We also describe herein that, in addition to intra-MRD heterogeneity, MRD's phenotypic composition is also subjected to marked interpatient variability. These observations pose several challenges when it comes to the rational targeting of MRD. One can envision two paradigms for targeting MRD. MRD-targeted treatments may be tailored to the particular MRD composition

of the individual patient. This will require sampling and characterization of MRD based on a simple method that can be implemented in routine diagnostic laboratories, use small amounts of input material and generate easily interpretable data. We describe a ''deconvolution'' method that is based on bulk RNA analysis, which predicts with accuracy the proportion of each of the four drug-tolerant states within a given MRD. This method could be amenable to the clinic to assess MRD and, ultimately, inform the rational selection of a second- or a third-line therapy. However, we also show that MRD exhibit geographic heterogeneity and therefore sampling from a single site could result in misinterpretation of the true composition *in situ*. Moreover, independent MRD from the same patient may undergo divergent evolution that leads to distinct therapeutic responses. Finally, invasive sampling methods will be required to analyze MRD from sites such as liver, lung or brain.

In the second, and more favorable, paradigm one universal treatment that is capable of eradicating MRD regardless of its composition may be applied. Note that complete eradication of MRD may not be necessary. There indeed may be some degree of interdependencies between these subpopulations. Also, not all residual cells are able to contribute to the development of a drug-resistant and heterogeneous tumor. For instance, cells that opted for the differentiation trajectory may not be able to re-enter the cell cycle and proliferate into diagnosable relapse. In contrast, targeting the population(s) of cells with stem cell-like properties is clearly necessary and might even be sufficient. Importantly, gene set enrichment analyses indicated that NCSCs are associated with cancer stem cell phenotypic traits. Consistently, we show that the NCSC subpopulation is a key driver of relapse.

SCENIC predicted RXRG as a key driver of the NCSC state. Remarkably, inhibiting this pathway with a pan-RXR antagonist (HX531) blocked the emergence of NCSCs in drug-exposed cultures. Combined with MAPK-targeting agents, the RXR antagonist also decreased the emergence of NCSCs in MRD and significantly delayed the onset of resistance. Importantly, this occurred despite HX only attenuating (but not preventing) emergence of NCSCs and promoting a concomitant increase in the other three drug-tolerant states in MRD. Therefore, these data highlight the critical role of the NCSC population in driving relapse and even raise the possibility that selective and more efficient targeting of the NCSC subpopulation in MRD may offer an effective approach for delaying or even preventing the development of resistance to melanoma targeted therapy. Noteworthy, HX treatment led to a particularly prominent increase in the AXL^{high} invasive subpopulation, the targeting of which is now possible through the use of the antibody-drug conjugate AXL-107-MMAE (Boshuizen et al., 2018). Therefore, it may be interesting to test whether adding this molecule to the aforementioned treatment regimen provides additional potential clinical benefit.

In conclusion, although our efforts to characterize MRD through single-cell profiling methods have highlighted an underappreciated heterogeneity and interpatient variability, they also demonstrate that a better understanding of the biology of a finite number of drug-tolerant states may constitute one of the next frontiers for improving outcomes among patients who achieve objective anti-tumor responses to specific anticancer drugs.

STAR★METHODS

Detailed methods are provided in the online version of this paper and include the following:

- KEY RESOURCES TABLE
- CONTACT FOR REAGENT AND RESOURCE SHARING
- EXPERIMENTAL MODEL AND SUBJECT DETAILS
  - Cell culturing
  - Patient-derived xenografts
  - Pharmacologic treatment of mice
  - Patient samples
- METHOD DETAILS
  - Immunohistochemistry
  - FACS
  - Single cell sorting
  - SMARTseq2
  - Library preparation and RNA-sequencing
  - RNA-seq analysis
  - SCENIC analysis
  - Diffusion map
  - RT-qPCR
  - Colony assay
  - CellTiter-Glo
  - EdU proliferation assay
  - TCGA analysis
  - Gene set enrichment analysis
  - Fluorescence *in situ* hybridization analysis
  - Bulk gene expression deconvolution
  - Single-cell DNA sequencing
  - Single-cell DNA analysis
  - Dropseq (10x Genomics)
  - Multiplexed, Sequential Immunohistochemistry and Analysis
- QUANTIFICATION AND STATISTICAL ANALYSIS
  - Quantification of gene sets per single cell
  - Sequential chromogenic immunohistochemistry
  - Single and double immunostainings
  - Statistical analyses
- DATA AND SOFTWARE AVAILABILITY

SUPPLEMENTAL INFORMATION

Supplemental Information includes seven figures and one table and can be found with this article online at https://doi.org/10.1016/j.cell.2018.06.025.

ACKNOWLEDGMENTS

We thank G. Bervoets for excellent technical assistance and Prof. G. Ghanem for the MM lines. M. Stas and V. Boecxstaens provided samples for the PDX models. PDX experiments were developed by TRACE with the assistance of E. Leucci, L. Rizzotto, F. Amant, E. Hermans, D. Thomas, E. Gommé, and K. Crevits. FACS was performed by P.A. Penttila and C. Nkama. The TruSight26 analysis was performed by S. Vander Borght. We thank the University Research Priority Program in translational cancer research for access to the melanoma material. D. Nittner and L. Omodho provided histology support. F.R. received a fellowship from the Omics/Marie Curie@VIB. This work was

supported by KUL GOA (#14/012), VLK (Vlaamse Liga tegen Kanker), Interreg (SKiN-HUID), and Fonds voor Wetenschappelijk Onderzoek Vlaanderen (#G.0929.16N). J.F. was supported by the Swedish Research Council. A.W.L. was supported by the OHSU Knight Cancer Center Support grant NIH P30-CA069533, the Department of Defense Peer Reviewed Cancer Research Program (W81XWH-15-1-0348), V Foundation for Cancer Research (V2015-024), and the Cancer Research Institute and Melanoma Research Alliance.

AUTHOR CONTRIBUTIONS

F.R. and A.R. designed and conducted the experiments and acquired, analyzed, and interpreted the data. S.A. analyzed data. J.F., Y.H.C., and A.W.L. performed multiplexed immunohistochemistry and analyzed and interpreted the results. O.M.-B., M.D., P.K., D.B., M.D.-R., C.A., and D.T.F. conducted the experiments and acquired the data. P.W., O.B., R.D., M.L., A.P., G.B., and K.T.F. provided valuable clinical samples and contributed to the analysis and the interpretation of the resultant data. E.R. and J.v.d.O. provided human pathology support. S.A. and T.V. interpreted the data. All authors read and edited the manuscript. F.R. and J.-C.M. conceptualized and designed the research study and wrote the manuscript.

DECLARATION OF INTERESTS

J.-C.M. and F.R. have a patent application pending (1st filling) related to this work.

Received: October 9, 2017
Revised: April 13, 2018
Accepted: June 12, 2018
Published: July 12, 2018

REFERENCES

Agarwal, P., Verzi, M.P., Nguyen, T., Hu, J., Ehlers, M.L., McCulley, D.J., Xu, S.M., Dodou, E., Anderson, J.P., Wei, M.L., and Black, B.L. (2011). The MADS box transcription factor MEF2C regulates melanocyte development and is a direct transcriptional target and partner of SOX10. Development *138*, 2555–2565.

Aibar, S., González-Blas, C.B., Moerman, T., Huynh-Thu, V.A., Imrichova, H., Hulselmans, G., Rambow, F., Marine, J.C., Geurts, P., Aerts, J., et al. (2017). SCENIC: single-cell regulatory network inference and clustering. Nat. Methods *14*, 1083–1086.

Anders, S., and Huber, W. (2010). Differential expression analysis for sequence count data. Genome Biol. *11*, R106.

Angerer, P., Haghverdi, L., Büttner, M., Theis, F.J., Marr, C., and Buettner, F. (2016). Destiny: diffusion maps for large-scale single-cell data in R. Bioinformatics *32*, 1241–1243.

Baslan, T., Kendall, J., Rodgers, L., Cox, H., Riggs, M., Stepansky, A., Troge, J., Ravi, K., Esposito, D., Lakshmi, B., et al. (2012). Genome-wide copy number analysis of single cells. Nat. Protoc. *7*, 1024–1041.

Boshuizen, J., Koopman, L.A., Krijgsman, O., Shahrabi, A., van den Heuvel, E.G., Ligtenberg, M.A., Vredevoogd, D.W., Kemper, K., Kuilman, T., Song, J.Y., et al. (2018). Cooperative targeting of melanoma heterogeneity with an AXL antibody-drug conjugate and BRAF/MEK inhibitors. Nat. Med. *24*, 203–212.

Chu, V.T., Gottardo, R., Raftery, A.E., Bumgarner, R.E., and Yeung, K.Y. (2008). MeV+R: using MeV as a graphical user interface for Bioconductor applications in microarray analysis. Genome Biol. *9*, R118.

Codega, P., Silva-Vargas, V., Paul, A., Maldonado-Soto, A.R., Deleo, A.M., Pastrana, E., and Doetsch, F. (2014). Prospective identification and purification of quiescent adult neural stem cells from their in vivo niche. Neuron *82*, 545–559.

Dobin, A., Davis, C.A., Schlesinger, F., Drenkow, J., Zaleski, C., Jha, S., Batut, P., Chaisson, M., and Gingeras, T.R. (2013). STAR: ultrafast universal RNA-seq aligner. Bioinformatics *29*, 15–21.

Ebisawa, M., Umemiya, H., Ohta, K., Fukasawa, H., Kawachi, E., Christoffel, G., Gronemeyer, H., Tsuji, M., Hashimoto, Y., Shudo, K., and Kagechika, H. (1999). Retinoid X receptor-antagonistic diazepinylbenzoic acids. Chem. Pharm. Bull. (Tokyo) *47*, 1778–1786.

Evans, R.M., and Mangelsdorf, D.J. (2014). Nuclear receptors, RXR, and the big bang. Cell *157*, 255–266.

Fallahi-Sichani, M., Becker, V., Izar, B., Baker, G.J., Lin, J.R., Boswell, S.A., Shah, P., Rotem, A., Garraway, L.A., and Sorger, P.K. (2017). Adaptive resistance of melanoma cells to RAF inhibition via reversible induction of a slowly dividing de-differentiated state. Mol. Syst. Biol. *13*, 905.

Fan, J., Salathia, N., Liu, R., Kaeser, G.E., Yung, Y.C., Herman, J.L., Kaper, F., Fan, J.B., Zhang, K., Chun, J., and Kharchenko, P.V. (2016). Characterizing transcriptional heterogeneity through pathway and gene set overdispersion analysis. Nat. Methods *13*, 241–244.

Gopal, Y.N., Rizos, H., Chen, G., Deng, W., Frederick, D.T., Cooper, Z.A., Scolyer, R.A., Pupo, G., Komurov, K., Sehgal, V., et al. (2014). Inhibition of mTORC1/2 overcomes resistance to MAPK pathway inhibitors mediated by PGC1α and oxidative phosphorylation in melanoma. Cancer Res. *74*, 7037–7047.

Haq, R., Shoag, J., Andreu-Perez, P., Yokoyama, S., Edelman, H., Rowe, G.C., Frederick, D.T., Hurley, A.D., Nellore, A., Kung, A.L., et al. (2013a). Oncogenic BRAF regulates oxidative metabolism via PGC1α and MITF. Cancer Cell *23*, 302–315.

Haq, R., Yokoyama, S., Hawryluk, E.B., Jönsson, G.B., Frederick, D.T., McHenry, K., Porter, D., Tran, T.N., Love, K.T., Langer, R., et al. (2013b). BCL2A1 is a lineage-specific antiapoptotic melanoma oncogene that confers resistance to BRAF inhibition. Proc. Natl. Acad. Sci. USA *110*, 4321–4326.

Hoek, K.S., Schlegel, N.C., Brafford, P., Sucker, A., Ugurel, S., Kumar, R., Weber, B.L., Nathanson, K.L., Phillips, D.J., Herlyn, M., et al. (2006). Metastatic potential of melanomas defined by specific gene expression profiles with no BRAF signature. Pigment Cell Res. *19*, 290–302.

Hoek, K.S., Eichhoff, O.M., Schlegel, N.C., Döbbeling, U., Kobert, N., Schaerer, L., Hemmi, S., and Dummer, R. (2008). In vivo switching of human melanoma cells between proliferative and invasive states. Cancer Res. *68*, 650–656.

Hu, J., Verzi, M.P., Robinson, A.S., Tang, P.L., Hua, L.L., Xu, S.M., Kwok, P.Y., and Black, B.L. (2015). Endothelin signaling activates Mef2c expression in the neural crest through a MEF2C-dependent positive-feedback transcriptional pathway. Development *142*, 2775–2780.

Huang, S. (2012). Tumor progression: chance and necessity in Darwinian and Lamarckian somatic (mutationless) evolution. Prog. Biophys. Mol. Biol. *110*, 69–86.

Ji, Z., Erin Chen, Y., Kumar, R., Taylor, M., Jenny Njauw, C.N., Miao, B., Frederick, D.T., Wargo, J.A., Flaherty, K.T., Jönsson, G., and Tsao, H. (2015). MITF modulates therapeutic resistance through EGFR signaling. J. Invest. Dermatol. *135*, 1863–1872.

Johannessen, C.M., Johnson, L.A., Piccioni, F., Townes, A., Frederick, D.T., Donahue, M.K., Narayan, R., Flaherty, K.T., Wargo, J.A., Root, D.E., and Garraway, L.A. (2013). A melanocyte lineage program confers resistance to MAP kinase pathway inhibition. Nature *504*, 138–142.

Kemper, K., de Goeje, P.L., Peeper, D.S., and van Amerongen, R. (2014). Phenotype switching: tumor cell plasticity as a resistance mechanism and target for therapy. Cancer Res. *74*, 5937–5941.

Kharchenko, P.V., Silberstein, L., and Scadden, D.T. (2014). Bayesian approach to single-cell differential expression analysis. Nat. Methods *11*, 740–742.

Kim, P., Cheng, F., Zhao, J., and Zhao, Z. (2016). ccmGDB: a database for cancer cell metabolism genes. Nucleic Acids Res. *44* (D1), D959–D968.

Konieczkowski, D.J., Johannessen, C.M., Abudayyeh, O., Kim, J.W., Cooper, Z.A., Piris, A., Frederick, D.T., Barzily-Rokni, M., Straussman, R., Haq, R., et al.

(2014). A melanoma cell state distinction influences sensitivity to MAPK pathway inhibitors. Cancer Discov. *4*, 816–827.

Llorens-Bobadilla, E., Zhao, S., Baser, A., Saiz-Castro, G., Zwadlo, K., and Martin-Villalba, A. (2015). Single-Cell transcriptomics reveals a population of dormant neural stem cells that become activated upon brain injury. Cell Stem Cell *17*, 329–340.

Long, G.V., Fung, C., Menzies, A.M., Pupo, G.M., Carlino, M.S., Hyman, J., Shahheydari, H., Tembe, V., Thompson, J.F., Saw, R.P., et al. (2014). Increased MAPK reactivation in early resistance to dabrafenib/trametinib combination therapy of BRAF-mutant metastatic melanoma. Nat. Comm. *5*, 5694.

Lun, A.T., McCarthy, D.J., and Marioni, J.C. (2016). A step-by-step workflow for low-level analysis of single-cell RNA-seq data with Bioconductor. F1000Res. *5*, 2122.

Luskin, M.R., Murakami, M.A., Manalis, S.R., and Weinstock, D.M. (2018). Targeting minimal residual disease: a path to cure? Nat. Rev. Cancer *18*, 255–263.

Macaulay, I.C., Teng, M.J., Haerty, W., Kumar, P., Ponting, C.P., and Voet, T. (2016). Separation and parallel sequencing of the genomes and transcriptomes of single cells using G&T-seq. Nat. Protoc. *11*, 2081–2103.

Martino, V.B., Sabljic, T., Deschamps, P., Green, R.M., Akula, M., Peacock, E., Ball, A., Williams, T., and West-Mays, J.A. (2016). Conditional deletion of AP-2β in mouse cranial neural crest results in anterior segment dysgenesis and early-onset glaucoma. Dis. Model. Mech. *9*, 849–861.

McCarthy, D.J., Campbell, K.R., Lun, A.T., and Wills, Q.F. (2017). Scater: pre-processing, quality control, normalization and visualization of single-cell RNA-seq data in R. Bioinformatics *33*, 1179–1186.

Menon, D.R., Das, S., Krepler, C., Vultur, A., Rinner, B., Schauer, S., Kashofer, K., Wagner, K., Zhang, G., Rad, E.B., et al. (2015). A stress-induced early innate response causes multidrug tolerance in melanoma. Oncogene *34*, 4545.

Müller, J., Krijgsman, O., Tsoi, J., Robert, L., Hugo, W., Song, C., Kong, X., Possik, P.A., Cornelissen-Steijger, P.D., Geukes Foppen, M.H., et al. (2014). Low MITF/AXL ratio predicts early resistance to multiple targeted drugs in melanoma. Nat. Commun. *5*, 5712.

Picelli, S., Faridani, O.R., Björklund, A.K., Winberg, G., Sagasser, S., and Sandberg, R. (2014). Full-length RNA-seq from single cells using Smart-seq2. Nat. Protoc. *9*, 171–181.

Pinto, J.P., Kalathur, R.K., Oliveira, D.V., Barata, T., Machado, R.S., Machado, S., Pacheco-Leyva, I., Duarte, I., and Futschik, M.E. (2015). StemChecker: a web-based tool to discover and explore stemness signatures in gene sets. Nucleic Acids Res. *43* (W1), W72–W77.

Pisco, A.O., and Huang, S. (2015). Non-genetic cancer cell plasticity and therapy-induced stemness in tumour relapse: 'What does not kill me strengthens me'. Br. J. Cancer *112*, 1725–1732.

Redmer, T., Welte, Y., Behrens, D., Fichtner, I., Przybilla, D., Wruck, W., Yaspo, M.L., Lehrach, H., Schäfer, R., and Regenbrecht, C.R. (2014). The nerve growth factor receptor CD271 is crucial to maintain tumorigenicity and stem-like properties of melanoma cells. PLoS ONE *9*, e92596.

Rizos, H., Menzies, A.M., Pupo, G.M., Carlino, M.S., Fung, C., Hyman, J., Haydu, L.E., Mijatov, B., Becker, T.M., Boyd, S.C., et al. (2014). BRAF inhibitor resistance mechanisms in metastatic melanoma: spectrum and clinical impact. Clin. Cancer Res. *20*, 1965–1977.

Roesch, A., Vultur, A., Bogeski, I., Wang, H., Zimmermann, K.M., Speicher, D., Körbel, C., Laschke, M.W., Gimotty, P.A., Philipp, S.E., et al. (2013). Overcoming intrinsic multidrug resistance in melanoma by blocking the mitochondrial respiratory chain of slow-cycling JARID1B(high) cells. Cancer Cell *23*, 811–825.

Shaffer, S.M., Dunagin, M.C., Torborg, S.R., Torre, E.A., Emert, B., Krepler, C., Beqiri, M., Sproesser, K., Brafford, P.A., Xiao, M., et al. (2017). Rare cell variability and drug-induced reprogramming as a mode of cancer drug resistance. Nature *546*, 431–435.

Sharma, S.V., Lee, D.Y., Li, B., Quinlan, M.P., Takahashi, F., Maheswaran, S., McDermott, U., Azizian, N., Zou, L., Fischbach, M.A., et al. (2010). A chromatin-mediated reversible drug-tolerant state in cancer cell subpopulations. Cell *141*, 69–80.

Smith, M.P., Brunton, H., Rowling, E.J., Ferguson, J., Arozarena, I., Miskolczi, Z., Lee, J.L., Girotti, M.R., Marais, R., Levesque, M.P., et al. (2016). Inhibiting drivers of non-mutational drug tolerance is a salvage strategy for targeted melanoma therapy. Cancer Cell *29*, 270–284.

Smith, M.P., Ferguson, J., Arozarena, I., Hayward, R., Marais, R., Chapman, A., Hurlstone, A., and Wellbrock, C. (2013). Effect of SMURF2 targeting on susceptibility to MEK inhibitors in melanoma. J. Natl. Cancer Inst. *105*, 33–46.

Su, Y., Wei, W., Robert, L., Xue, M., Tsoi, J., Garcia-Diaz, A., Homet Moreno, B., Kim, J., Ng, R.H., Lee, J.W., et al. (2017). Single-cell analysis resolves the cell state transition and signaling dynamics associated with melanoma drug-induced resistance. Proc. Natl. Acad. Sci. USA *114*, 13679–13684.

Tirosh, I., Izar, B., Prakadan, S.M., Wadsworth, M.H., 2nd, Treacy, D., Trombetta, J.J., Rotem, A., Rodman, C., Lian, C., Murphy, G., et al. (2016). Dissecting the multicellular ecosystem of metastatic melanoma by single-cell RNA-seq. Science *352*, 189–196.

Titz, B., Lomova, A., Le, A., Hugo, W., Kong, X., Ten Hoeve, J., Friedman, M., Shi, H., Moriceau, G., Song, C., et al. (2016). JUN dependency in distinct early and late BRAF inhibition adaptation states of melanoma. Cell Discov. *2*, 16028.

Trapnell, C., Cacchiarelli, D., Grimsby, J., Pokharel, P., Li, S., Morse, M., Lennon, N.J., Livak, K.J., Mikkelsen, T.S., and Rinn, J.L. (2014). The dynamics and regulators of cell fate decisions are revealed by pseudotemporal ordering of single cells. Nat. Biotechnol. *32*, 381–386.

Trumpp, A., and Wiestler, O.D. (2008). Mechanisms of disease: cancer stem cells–targeting the evil twin. Nat. Clin. Pract. Oncol. *5*, 337–347.

Tsujikawa, T., Kumar, S., Borkar, R.N., Azimi, V., Thibault, G., Chang, Y.H., Balter, A., Kawashima, R., Choe, G., Sauer, D., et al. (2017). Quantitative multiplex immunohistochemistry reveals myeloid-inflamed tumor-immune complexity associated with poor prognosis. Cell Rep. *19*, 203–217.

Van Allen, E.M., Wagle, N., Sucker, A., Treacy, D.J., Johannessen, C.M., Goetz, E.M., Place, C.S., Taylor-Weiner, A., Whittaker, S., Kryukov, G.V., et al.; Dermatologic Cooperative Oncology Group of Germany (DeCOG) (2014). The genetic landscape of clinical resistance to RAF inhibition in metastatic melanoma. Cancer Discov. *4*, 94–109.

Verfaillie, A., Imrichova, H., Atak, Z.K., Dewaele, M., Rambow, F., Hulselmans, G., Christiaens, V., Svetlichnyy, D., Luciani, F., Van den Mooter, L., et al. (2015). Decoding the regulatory landscape of melanoma reveals TEADS as regulators of the invasive cell state. Nat. Commun. *6*, 6683.

Verhaak, R.G., Hoadley, K.A., Purdom, E., Wang, V., Qi, Y., Wilkerson, M.D., Miller, C.R., Ding, L., Golub, T., Mesirov, J.P., et al.; Cancer Genome Atlas Research Network (2010). Integrated genomic analysis identifies clinically relevant subtypes of glioblastoma characterized by abnormalities in PDGFRA, IDH1, EGFR, and NF1. Cancer Cell *17*, 98–110.

Wellbrock, C., and Arozarena, I. (2015). Microphthalmia-associated transcription factor in melanoma development and MAP-kinase pathway targeted therapy. Pigment Cell Melanoma Res. *28*, 390–406.

Please cite this article in press as: Rambow et al., Toward Minimal Residual Disease-Directed Therapy in Melanoma, Cell (2018), https://doi.org/10.1016/j.cell.2018.06.025

STAR★METHODS

KEY RESOURCES TABLE

REAGENT or RESOURCE	SOURCE	IDENTIFIER
Antibodies		
Rabbit polyclonal anti-RXRG	Abcam	Cat#ab15518
Rabbit polyclonal anti-pERK	Cell Signaling	Cat#4370
Rabbit polyclonal anti-NGFR	Cell Signaling	Cat#8238
Rabbit polyclonal anti-S100	DAKO	Cat#Z0311
Rabbit polyclonal anti-AQP1	Millipore	Cat#AB2219
Goat polyclonal anti-AXL	R&D	Cat#AF154
Goat polyclonal anti-GFRA2	R&D	Cat#AF429
Goat polyclonal anti-MITF	R&D	Cat#AF5769
Goat polyclonal anti-SOX10	Santa Cruz	Cat#sc-17342
Rabbit polyclonal anti-CD36	Sigma-Aldrich	Cat#HPA002018
Rabbit polyclonal anti-MITF	Sigma-Aldrich	Cat#HPA003259
Rabbit polyclonal anti-MEF2C	Sigma-Aldrich	Cat#HPA005533
Rabbit polyclonal anti-TFAP2B	Sigma-Aldrich	Cat#HPA034683
Rabbit polyclonal anti-MLANA	Sigma-Aldrich	Cat#HPA048662
Donkey anti-goat Alexa Fluor 594	Thermo Fisher Scientific	Cat#A-11058
Donkey anti-rabbit Alexa Fluor 488	Thermo Fisher Scientific	Cat#A-21206
Rabbit polyclonal anti-Ki67	Thermo Fisher Scientific	Cat#RM-9106-S0
Donkey Anti-Rabbit IgG Unconjugated	Jackson Immunoresearch	Cat#711-007-003
Donkey anti-rabbit Fab fragment Alexa Fluor 488	Jackson Immunoresearch	Cat#111-547-003
Donkey anti-rabbit Fab fragment Alexa Fluor 594	Jackson Immunoresearch	Cat#711-587-003
Bacterial and Virus Strains		
dsRed encoding viral vector, pHR'SINcPPT-SGW RFP (VSV-G typed lentivirus, packed with third generation packaging constructs)	Laboratory for Translational Research in GastroIntestinal Disorders	N/A
Biological Samples		
Patient biopsies	Massachusetts General Hospital	https://www.massgeneral.org/
Patient biopsies	University of Zürich Hospital	http://www.en.usz.ch/Pages/default.aspx
Patient-derived xenografts (PDXs)	KU Leuven	https://www.uzleuven-kuleuven.be/lki/trace/
Chemicals, Peptides, and Recombinant Proteins		
Agencourt AMPure XP beads	Agencourt/ Beckman coulter	Cat#A63881
Bexarotene	MCE	Cat#HY-14171
Dabrafenib	MCE	Cat#HY-14660
Trametinib	MCE	Cat#HY-10999
Normal Donkey Serum	Jackson Immuneresearch	Cat#017-000-121
Collagenase Type I	Sigma-Aldrich	Cat#C0130
Collagenase Type IV	Sigma-Aldrich	Cat#C5138
KAPA HiFi Hot start Readymix	Sopachem	Cat#KK2602
Superscript II	Thermo Fisher Scientific	Cat#10328062
SYTOX Blue	Thermo Fisher Scientific	Cat#S34857
Trypsin (0.25%)	Thermo Fisher Scientific	Cat#25200056
DAPI (4',6-Diamidino-2-Phenylindole, Dilactate)	Thermo Fisher Scientific	Cat#D3571
HX531	Tocris	Cat#3912
F-10 Nut Mix (Ham)	GIBCO	Cat#22390-025

(*Continued on next page*)

Continued

REAGENT or RESOURCE	SOURCE	IDENTIFIER
RPMI Medium 1640	GIBCO	Cat#61870-010
DMEM/F-12	GIBCO	Cat#11039-021
FBS	GIBCO	Cat#10270-106
GlutaMAX	GIBCO	Cat#35050-038
Amphotericin B	GIBCO	*Cat#15290-018*
Penicillin/streptomycin	GIBCO	Cat#15140-122
Vectashield Antifade Mounting Medium	Vector Labs	Cat#H-1000
XCE2-SG probe	MetaSystems	Cat#D-0802-050-FI
Critical Commercial Assays		
Nextera XT library Prep Kit	Illumina	Cat#FC-131-1096
Nextera XT Index Kit v2 Set A	Illumina	Cat#FC-131-2001
Nextera XT Index Kit v2 Set B	Illumina	Cat#FC-131-2002
Nextera XT Index Kit v2 Set C	Illumina	Cat#FC-131-2003
Nextera XT Index Kit v2 Set D	Illumina	Cat#FC-131-2004
Chromium Single Cell A Chip	10x genomics	Cat#120236
Chromium i7 Multiplex kit	10x genomics	Cat#120262
Chromium Single Cell 3′ Library & Gel Bead Kit v2	10x genomics	Cat#120237
ImmPress HRP Anti-Rabbit Ig (Peroxidase)	Vector Labs	Cat#MP-7401
ImmPress HRP Anti-Goat Ig (Peroxidase)	Vector Labs	Cat#MP-7405
AEC Peroxidase substrate kit	Vector Labs	Cat#SK-4200
Click-iT Plus EdU Alexa Fluor 647 Flow Cytometry Assay Kit	Thermo Fisher Scientific	Cat#C10634
Deposited Data		
GEO accession number pending	N/A	GEO: GSE116237
Experimental Models: Cell Lines		
MM052	Prof. G. Ghanem, LOCE-institut J. Bordet, Université Libre de Bruxelles	N/A
MM165	Prof. G. Ghanem, LOCE-institut J. Bordet, Université Libre de Bruxelles	N/A
MM163	Prof. G. Ghanem, LOCE-institut J. Bordet, Université Libre de Bruxelles	N/A
MM099	Prof. G. Ghanem, LOCE-institut J. Bordet, Université Libre de Bruxelles	N/A
MM074	Prof. G. Ghanem, LOCE-institut J. Bordet, Université Libre de Bruxelles	N/A
MM029	Prof. G. Ghanem, LOCE-institut J. Bordet, Université Libre de Bruxelles	N/A
MM001	Prof. G. Ghanem, LOCE-institut J. Bordet, Université Libre de Bruxelles	N/A
MM011	Prof. G. Ghanem, LOCE-institut J. Bordet, Université Libre de Bruxelles	N/A
MM034	Prof. G. Ghanem, LOCE-institut J. Bordet, Université Libre de Bruxelles	N/A
MM118	Prof. G. Ghanem, LOCE-institut J. Bordet, Université Libre de Bruxelles	N/A
MM047	Prof. G. Ghanem, LOCE-institut J. Bordet, Université Libre de Bruxelles	N/A
MM057	Prof. G. Ghanem, LOCE-institut J. Bordet, Université Libre de Bruxelles	N/A

(*Continued on next page*)

Continued

REAGENT or RESOURCE	SOURCE	IDENTIFIER
MM087	Prof. G. Ghanem, LOCE-institut J. Bordet, Université Libre de Bruxelles	N/A
MM162	Prof. G. Ghanem, LOCE-institut J. Bordet, Université Libre de Bruxelles	N/A
MM032	Prof. G. Ghanem, LOCE-institut J. Bordet, Université Libre de Bruxelles	N/A
MM031	Prof. G. Ghanem, LOCE-institut J. Bordet, Université Libre de Bruxelles	N/A
Experimental Models: Organisms/Strains		
NMRI nude BomTac:NMRI-*Foxn1*^{nu}	Taconic	https://www.taconic.com/mouse-model/nmri-nude
SCID beige C.B-*Igh*-1b/GbmsTac-*Prkdc*^{scid}-*Lyst*^{bg} N7	Taconic	https://www.taconic.com/mouse-model/scid-beige
Oligonucleotides		
Primers for alternatively spliced BRAF: F-GGCTCTCGGTTATAAGATGGC	Long et al., 2014	N/A
Primers for alternatively spliced BRAF: R-ACAGGAAACGCACCATATCC	Long et al., 2014	N/A
Software and Algorithms		
DEseq2	Anders and Huber, 2010	https://bioconductor.org/packages/release/bioc/html/DESeq2.html
SCENIC	Aibar et al., 2017	https://github.com/aertslab/SCENIC
MeV (4_8 Version 10.2)	Chu et al., 2008	http://www.tm4.org/
SCDE (2.4.1)	Kharchenko et al., 2014	https://bioconductor.org/packages/release/bioc/html/scde.html
GraphPad Prism 7	GraphPad Software	https://www.graphpad.com/scientific-software/prism/
STAR RNaseq mapping	Dobin et al., 2013	https://github.com/alexdobin/STAR/releases
Monocle	Trapnell et al., 2014	https://bioconductor.org/packages/release/bioc/html/monocle.html
Destiny diffusion maps	Angerer et al., 2016	http://bioconductor.org/packages/release/bioc/html/destiny.html
Scater	McCarthy et al., 2017	https://bioconductor.org/packages/release/bioc/html/scater.html
R 3.3.3	R Project	https://www.r-project.org/
StemChecker	Pinto et al., 2015	http://stemchecker.sysbiolab.eu/
Cell Ranger R Kit	10x Genomics	https://support.10xgenomics.com/single-cell-gene-expression/software/pipelines/latest/rkit

CONTACT FOR REAGENT AND RESOURCE SHARING

Further information and requests for resources and reagents may be directed to and will be fulfilled by the lead contact, Jean-Christophe Marine (jeanchristophe.marine@kuleuven.vib.be).

EXPERIMENTAL MODEL AND SUBJECT DETAILS

Cell culturing

Cells from dissociated MEL006 tumors and melanoma short term cultures were grown in 5% CO2 at 37°C in F10 supplemented with 10% FBS and 0.25% GlutaMAX. Gender of the patients from whom the short-term cultures were derived (female: F; male: M): MM001: F; MM011: F; MM029: M; MM031: M; MM032: F; MM034: F; MM047: M; MM052: M; MM057: F; MM074: F; MM087: F; MM099: M; MM118: F; MM162: M; MM163: F; MM165: M.

Patient-derived xenografts

In collaboration with TRACE, patient-derived xenografts (PDX) models were established using tissue from patients undergoing surgery as part of standard-of-care melanoma treatment at the University Hospitals KU Leuven. Written informed consent was obtained from all patients and all procedures involving human samples were approved by the UZ Leuven Medical Ethical Committee (S54185/S57760/S59199) and carried out in accordance with the principles of the Declaration of Helsinki. PDX models MEL006, MEL015 and MEL007 were derived from a female, male and male patient respectively. All procedures involving animals were performed in accordance with the guidelines of the IACUC and KU Leuven and were carried out within the context of approved project applications P147/2012, P038/2015, P098/2015 and P035/2016. Fresh tumor tissue was collected in transport medium (RPMI1640 medium supplemented with penicillin/streptomycin and amphotericin B). Tumor fragments were subsequently rinsed in phosphate-buffered saline supplemented with penicillin/streptomycin and amphotericin B and cut into small pieces of approximately 3 × 3 x 3 mm^3. Tumor pieces were implanted subcutaneously in the interscapular fat pad of female SCID-beige mice (Taconic). Sedation and analgesia was performed using ketamine, medetomidine and buprenorphine. After reaching generation 4 (F4), one mouse with a tumor of 1000 mm^3 was sacrificed. This tumor was minced followed by dissociation using collagenase I & IV and trypsin. Cells were resuspended in serum-free DMEM/F12 medium and 250 000 cells were injected in the interscapular fat pad of 8 – 16 week old female NMRI nude mice (Taconic). For single cell RNA sequencing purposes, cells were transduced with a lentivirus carrying dsRed. Cells were washed four times before injecting into the interscapular fat pad. For immunohistochemistry, non-dsRed-transduced lesions were used. For FACS, tumors were enzymatically dissociated using the same protocol.

Pharmacologic treatment of mice

Mice with tumors reaching 1000 mm^3 were started on the BRAF-MEK combination via daily oral gavage. BRAF inhibitor dabrafenib and MEK inhibitor trametinib were dissolved in DMSO at a concentration of 30 and 0.3 mg/mL respectively, aliquoted and stored at −80°C. Each day a fresh aliquot was thawed and diluted 1:10 with phosphate-buffered saline. Mice were treated with a capped dose of 600 – 6 μg dabrafenib – trametinib respectively in 200 μL total volume. For the dabrafenib-trametinib-bexarotene and dabrafenib-trametinib-HX531 preparation, bexarotene was dissolved at 30 mg/mL and HX531 at 10 mg/dL respectively in combination with dabrafenib and trametinib. Tumor volume was monitored with a caliper and the volume was calculated using the following formula: V = (π/6)*length*width*height.

Patient samples

Melanoma samples from Zürich were obtained from surplus biopsies stored in the melanoma biobank at the University of Zurich Hospital. The patients consented to the use of their biopsy material for scientific studies (EK.647/800) and all research was conducted according to the standards established by the Declaration of Helsinki and abiding by all local laws for research on human derived tissue. Gender (female: F; male: M) of the reported samples: 16: M; 35: F; 409: F; 6: F; 12: F; 19: M; 42: M; 7: M; 13: M; 10: F; 34: M; 9: M; 3: F; 4: M; 5: F; 66: F.

METHOD DETAILS

Immunohistochemistry

Tumor biopsies were formalin-fixed, paraffin embedded and cut in sections of about 5 μm. Samples were deparaffinized and dehydrated with xylene and graded alcohols, and subsequently rehydrated with demineralized water. Immunostainings were performed with antibodies listed in the Key Resources Table. Fontana-Masson silver method histochemistry was performed with working silver solution and fast red counterstain. Image acquisition over larger areas of multiple continuous fields involved tiling and stitching performed with ZEN2 software after scanning with a Zeiss Axio Scan Z1 using x20 and x40 objectives. Microscopy images were brightness and contrast adjusted.

FACS

Cells were incubated with GFRA2 antibody AF429 (STAR Methods) for 45 minutes at room temperature, followed by a secondary antibody conjugated with Alexa Fluor® 594 (STAR Methods) for 30 min at room temperature. Cells were resuspended in FACS sorting buffer (culture medium supplied with 5% serum and 2 mM EDTA). FACS analyses were performed with BD FACSAria III and FlowJo® software.

Single cell sorting

SYTOX Blue negative, dsRed positive single cells were sorted (BD FACSAria III) in 96 well plates (VWR, DNase, RNase free) containing 2 μL of lysis buffer (0.2% Triton X-100, 4U of RNase inhibitor, Takara) per well. Plates were properly sealed and spun down at 2000 g for 1 min before storing at −80°C.

SMARTseq2

Whole transcriptome amplification was performed with a modified SMART-seq2 protocol as described previously (Picelli et al., 2014), using 20 instead of 18 cycles of cDNA amplification. PCR purification was realized with a 0.8:1 ratio (ampureXP beads:DNA). Amplified cDNA quality was monitored with a high sensitivity DNA chip (Agilent) using the Bioanalyzer (Agilent).

Library preparation and RNA-sequencing

Sequencing libraries were performed using the Nextera XT kit (Illumina) as described previously (Picelli et al., 2014), using 1/4th of the recommended reagent volumes and 1/5th of input DNA with a tagmentation time of 9 min. Library quality was monitored with a high sensitivity DNA chip (Agilent) using the Bioanalyzer (Agilent). Indexing was performed with the Nextera XT index Kit V2 (A-D). Up to 4x96 single cells were pooled per sequencing lane. Samples were sequenced on the Illumina NextSeq 500 platform using 75bp single-end reads.

RNA-seq analysis

BAM files were converted to merged, demultiplexed FASTQ files, cleaned using fastq-m*cf.* (ea-utils r819), and QC checked with FastQC (0.11.4). Reads were then mapped to the human genome (hg19) using STAR (2.4.1b) and quantified with Subread (1.4.6-p2). Cells with less than 100,000 reads and/or 1000 genes expressed were discarded. Furthermore, only cells with an average expression level > 3 of a curated list of housekeeping genes (n = 85) were kept (Tirosh et al., 2016). 760 of 937 sequenced cells passed these quality criteria. Subsequently, we applied an even more stringent workflow to detect low-quality cells based on: library size, genes expressed per cell, ERCCs, house-keeping gene expression and mitochondrial DNA reads (Lun et al., 2016). This resulted in 674 high-quality cells that were used for downstream analyses.

Next, we identified Highly Variable genes (HVGs) per time point following the Kharchenko pipeline (Kharchenko et al., 2014) (Table S1A): library size factor normalization (DESeq) and winsorization of the data prior plotting variation (logCV2) over mean expression (logmeans). After fitting a regression line to the data, genes were ranked and selected by their significance of deviation from the fit (adj. p value < 1e-3). For each time point, single cells were clustered in an unsupervised manner based on the expression of corresponding HVGs using non-negative matrix factorization as dimension reduction approach (run = 40, rank = 10, in MeV 4.8.1). The "best fit" (numbers of clusters) was chosen based on the highest cophenetic correlation coefficient. Next, Single-cell Differential Expression analysis (SCDE) was performed between the different NMF-clusters using the global gene expression matrix (Kharchenko et al., 2014). SCDE analysis generated a Z-score ranked gene list for each NMF cluster (n = 10) of which the top 100 candidates (Table S1B) were interpreted by Ingenuity Pathway Analysis (IPA) and i-cisTarget.

Characteristic gene signatures per NMF cluster were established by combining genes of highly enriched IPA and/or i-cisTarget terms (Table S1C) into 6 final gene signatures (Table S1D). To measure the activity of the 6 final gene signatures in each cell, we used the AUCell algorithm (Aibar et al., 2017). The activity of each of the 6 final signatures was visualized by i) projecting all 674 cells into a two-dimensional space using t-distributed stochastic neighbor embedding (t-SNE, perplexity = 30, initial_dims = 10, max_iter = 1000) based on the expression of all genes in the 6 final signatures (n = 284 unique genes) and ii) coloring cells according to their binary AUCell score.

SCENIC analysis

The SCENIC analysis was run as described in Aibar et al. (SCENIC version 0.1.5, which corresponds to GENIE3 0.99.3, RcisTarget 0.99.0 and AUCell 0.99.5) using the 20-thousand motifs database for RcisTarget (RcisTarget.hg19.motifDatabases.20k). The input matrix was the size-factor normalized expression matrix, from which 12255 genes passed the default filtering (rowSums > 5*0.03*760 and detected in at least 1% of the cells). From these genes, only the protein coding genes were kept in the co-expression modules from GENIE3 and analyzed for motif enrichment with RcisTarget.

Diffusion map

The diffusion maps were plotted through R/Bioconductor package destiny (version 2.0.8), centering and scaling the the size-factor normalized expression matrix including 557 cells (41 invasive, 44 neuro, 30 pigmented, and 442 MITFmedium) and the 1397 genes in any of the 4 signatures (units: log2(sfNormMat+1)).

RT-qPCR

Cells resuspended in QIAzol using an miRNeasy Kit and processed according to the manufacturer's instructions (QIAGEN) or in RA1 lysis buffer using the RNA NucleoSpin extraction kit (Macherey&Nagel). RNA was quantified using a NanoDrop 1000 (Thermo Scientific) and 500–2,000 ng was reverse transcribed with a High-Capacity cDNA Reverse Transcription Kit (Life Technologies). qPCRs were run using Fast SYBR Green Master Mix or SensiFast kit (Bioline) and a Roche LightCycler 384 (both from Life

Technologies). Data processing with qbase+ 2.6 software (Biogazelle) relies on normalization with a minimum of 2 reference genes. RT-qPCR primer sequences are available upon request.

Colony assay

Cells were grown to near confluency on 12 well plates and treated with the indicated drug combinations for the indicated time period. Cells were washed once with PBS, stained with crystal violet (1% crystal violet w/v, 35% methanol v/v) for 15 min, washed with PBS and destained in tap water.

CellTiter-Glo

2500 cells were plated onto a 96 well plate and treated with the indicated drug combinations for the indicated time period. CellTiter-Glo assay was performed according to the manufacturer's instructions (Promega) and luminescence was measured on a VictorX3 (Perkin Elmer).

EdU proliferation assay

Cells were pulsed for 35 minutes with 10 μM EdU, washed and fixed. After overnight incubation with BD Perm/Wash buffer, cells were stained for 30 min with Click-IT cocktail, counterstained with DAPI and slides were mounted (Vectashield Mounting Medium). Imaging was performed using a Nikon A1 confocal microscope. Total number of cell nuclei and EdU positive cells per field were counted using Fiji software.

TCGA analysis

GFRA2 and AQP1 RNA expression levels were quantified (RSEM normalized reads) in 470 melanoma patients (TCGA_SKCM) using the RNaseq explorer (http://tcgabrowser.ethz.ch:3839/TEST/). Differential gene expression analysis between highest and lowest GFRA2 and AQP1 expressers (7th percentile) was performed, genes and patients were hierarchically clustered and a selection of co-differentially expressed genes plotted as heatmap.

Gene set enrichment analysis

Gene set enrichment analysis (GSEA version 2.2.1) was performed by ranking SCDE genes based on their cZ-score as metric. Different ranked SCDE lists were used including MITF-medium comparison, NCSC versus invasive, and NCSC versus other comparison. The following gene signatures were analyzed for enrichment: proliferative melanoma (433 genes, FC > 3) (Verfaillie et al., 2015), cancer cell metabolism gene database (2071 genes) (Kim et al., 2016), GO_neural crest_cell_differentiation (75 genes, MSigDB), quiescent neural stem cells (324 genes) Llorens-Bobadilla et al., 2015), glioblastoma proneural (178 genes) (Verhaak et al., 2010), KEGG_Focal adhesion (201 genes, MSigDB), quiescent neural stem cells (216 genes) (Codega et al., 2014), drug tolerant persistors PC-9 cells (233 genes, FC > 3) (Sharma et al., 2010), top 100 upregulated genes in FACS sorted GFRA2+ cells *in vitro*.

Fluorescence *in situ* hybridization analysis

Interphase fluorescence *in situ* hybridization (FISH) was performed on 5-μm paraffin sections of formalin fixed (FFPE) xenograft tumor specimens applying the Spectrum Green-labeled chromosome 2 centromeric probe (XCE2-SG; Meta Systems Probes, Altlussheim, Germany). Briefly, FFPE sections were deparaffinized in three changes of xylenes, dehydrated in ethanol, pretreated in sodium thiocyanate buffer (Abbott Molecular, Abbott Park, IL) for 30 minutes at 80°C, followed by pepsin digestion for 25 minutes at 37°C. Hybridization was performed at 37°C overnight. Slides were then washed and mounted with DAPI in an antifade solution. The number of green signals was analyzed in 300 hundred successive, non-overlapping tumor cell nuclei using a Zeiss fluorescence microscope (Zeiss Axioplan, Oberkochen, Germany), controlled by Isis 5 software (Metasystems, Newton, MA).

Bulk gene expression deconvolution

For human melanoma patients, RSEM gene-level estimated counts from bulk RNA sequencing were retrieved for discriminative DTC specific marker genes (6-7 genes per DTC state). Gene expression changes were quantified by comparing matched samples of ON versus pre-treatment samples. Per DTC state, gene expression changes were averaged. For PDX samples, DTC related gene expression changes were assessed by RT-qPCR (6-7 marker genes per state). As mentioned before, PDX samples ON treatment (during MRD) were compared to pre-treatment counterparts. Per DTC state, gene expression changes were averaged (pigmented state markers: MITF, MLANA, DCT, TRPM1, TYR; SMC state markers: CD36, DLX5, IP6K3, PAX3, TRIM67; invasive state markers: AXL, CYR61, LOXL2, TCF4, TNC, WNT5A; NCSC state markers: AQP1, GFRA2, L1CAM, NGFR, SLC22A17, TMEM176B).

Single-cell DNA sequencing

Sorting was performed as for the single-cell RNA-seq experiments. dsRed positive single-cells were sorted into 2.5 μL of RLT plus buffer (QIAGEN 1053393), snap frozen on dry ice and stored at −80°C. Subsequently, the single cells' DNA was purified and amplified using Picoplex (Rubicon R30050) following established (Macaulay et al., 2016). The amplified DNA was purified using 0.8x ratio of AMPure XP beads using a Hamilton robot and subsequently quantified using a QuantiFluor dsDNA System (Promega E2670). 100pg of amplified DNA was used to prepare Illumina sequencing libraries using a Nextera XT DNA sample preparation kit (Illumina

FC-131-1096) with volumes reduced by one-tenth on a Labcyte Echo 525 liquid handling robot (Labcyte). After PCR, all samples were pooled and purified using AMPure XP beads at a 0.6x ratio. Library pools were eluted in buffer EB and quality control performed using an Agilent 2100 BioAnalyzer and High Sensitivity DNA chip before adjusting to a concentration of 4nM. The diluted pools were quantified using a KAPA qPCR library quantification kit 480 (Roche 7960140001) on a LightCycler 480 before a final dilution to 1.5nM. Sequencing was performed on HiSeq4000 with 50bp single-end reads.

Single-cell DNA analysis

Sequencing reads were aligned to the GRCh37 human reference using Burrows-Wheeler Aligner (BWA). LogR values were calculated for genomic bins of 500,000 uniquely mappable positions, maintaining unique reads with a minimum mapping quality of 30 (Baslan et al., 2012). A value of 1 was added to each bin's single-cell read count and bins with a %GC content less than 28% were discarded. The bin counts were then transformed by taking the log2 ratio (logR) per bin by dividing the read count of a given bin by the median read count of the bins genome-wide. LogR values were corrected for GC bias using a Loess fit and normalized to the median of the genome-wide logR value. The normalized LogR values were finally segmented using piecewise constant fitting (with the penalty parameter γ set to 15). Cells with a median absolute pairwise difference (MAPD) greater than 0.6 were discarded from the analysis resulting in 95 T0 and 84 phase 2-cells passing quality control.

Dropseq (10x Genomics)

We loaded ~8,700 cells into one channel of the Chromium system using the v2 single cell reagent kit (10X Genomics). Following capture and lysis, we synthesized cDNA and amplified for 12 cycles. The amplified cDNA was used to construct Illumina sequencing libraries that were each sequenced on an Illumina Nextseq500.

Multiplexed, Sequential Immunohistochemistry and Analysis

Sequential chromogenic immunohistochemistry was performed as previously described (Tsujikawa et al., 2017), using a modified protocol. In brief, 5 μm FFPE tissue sections of human primary melanoma were de-paraffinized and subsequently stained with hematoxylin (GHS116, Sigma-Aldrich) to visualize nuclei. Following whole-tissue scanning using Aperio ImageScope AT (Leica Biosystems), iterative cycles of standard IHC were performed followed by detection with ImmPressTM IgG-polymerized peroxidase reagents (Vector Laboratories) and visualization with AEC (Vector Laboratories). After whole tissue scanning, AEC was removed using ethanol, antibody was stripped in heated citrate buffer, and the next staining cycle with the next primary antibody was performed. Serial digitized images were processed using a computational image analysis workflow described previously (Tsujikawa et al., 2017) to align and visualize several markers simultaneously in a single pseudo-colored image. From whole-tissue serial images rectangular regions of interest with an area of 6.25 mm^2 were selected.

QUANTIFICATION AND STATISTICAL ANALYSIS

Quantification of gene sets per single cell

We used AUCell to quantify our different gene sets per single cell (Aibar et al., 2017). Briefly, the AUCell output is the gene set 'activity' in each cell (score: 0-1). AUCell calculates the enrichment of the gene sets as an area under the recovery curve (AUC) across the ranking of all genes in a particular cell, whereby genes are ranked by their expression value. This method is independent of the gene expression units and the normalization procedure. AUCell then uses the AUC to calculate whether a critical subset of the input gene set is enriched at the top of the ranking for each cell. In this way, the AUC represents the proportion of expressed genes in the signature and their relative expression values compared to the other genes within the cell (R-packages: SCENIC version 0.1.5, which corresponds to GENIE3 0.99.3, RcisTarget 0.99.0 and AUCell 0.99.5).

Sequential chromogenic immunohistochemistry

Single-cell segmentation and quantification of staining intensity was performed using a CellProfiler v.2.1.1 pipeline. Pixel intensity and shape-size measurements were compatibility with image cytometry data analysis software, FCS Express 5 Image Cytometry v.5.01.0029 (*De Novo* Software) used for setting gate thresholds for subsequent analysis.

Single and double immunostainings

Figures 3B, 3D, 5H, 6C, S3B, S4B, and S7D were manually counted by an independent expert to allow for the exclusion of AQP1-expressing endothelial cells on morphological grounds. Panels associated with these AQP1 quantifications were processed identically for reasons of consistency. Figure 5H was quantified using Fiji software to manually count EdU positive cells and to determine total numbers of nuclei per field.

Statistical analyses

Statistical comparisons in Figures 1C, 5H, and 7A were carried out using the non-parametric Mann-Whitney test. The statistical comparison in Figure 6A was done using the hypergeometric distribution test and the Mantel-Cox log-rank test was used to statistically compare time to progression in Figure 7G. Throughout all figures: significance was concluded at $p < 0.05$ (*$p < 0.05$, **$p < 0.01$, and ***$p < 0.001$).

DATA AND SOFTWARE AVAILABILITY

The accession number for the RNA and DNaseq data reported in this paper is GEO: GSE116237.

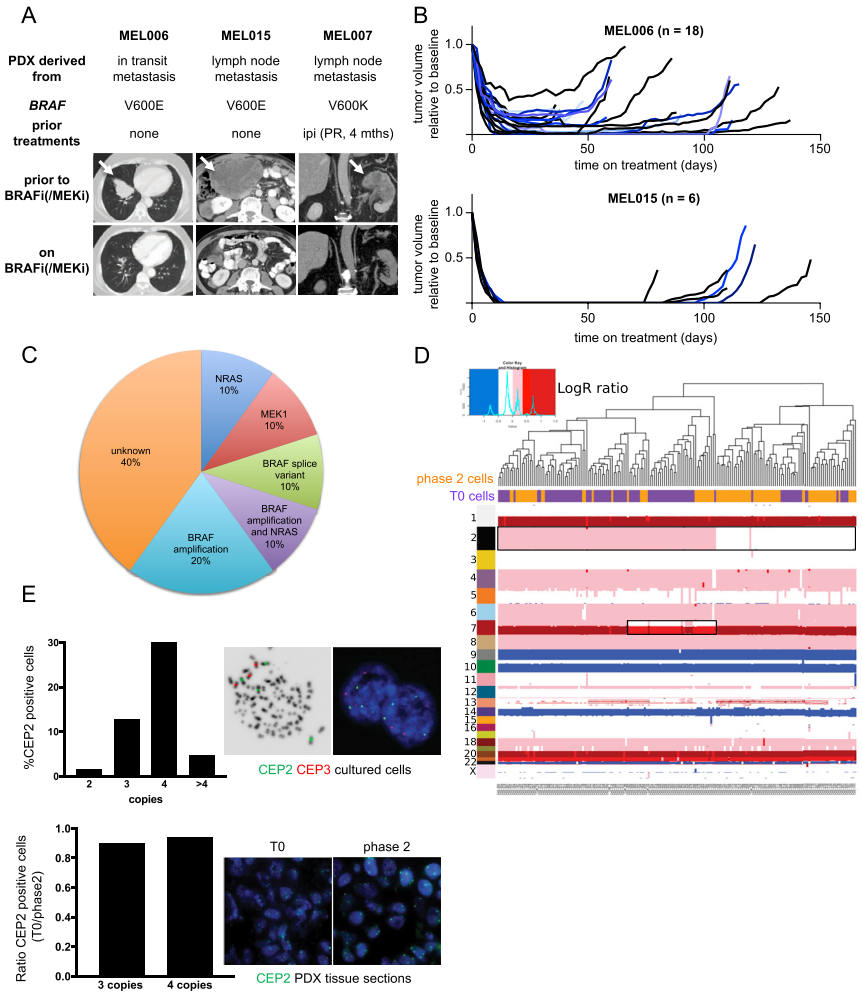

Figure S1. Establishment of Melanoma PDX Models and Their Response to BRAF&MEK Inhibition, Related to Figure 1

(A) Information about the three BRAF mutant PDX melanoma models MEL006, MEL015 and MEL007: site from which the initial lesions were obtained, *BRAF* mutation status, treatments prior to establishing the PDX model. Patient MEL006 achieved an almost complete response to dabrafenib-trametinib. Patient MEL015 and MEL007 had a partial response to dabrafenib-trametinib and vemurafenib, respectively. Computed tomography (CT) images depict a responding lung, intra-abdominal and kidney metastasis in patients MEL006, MEL015 and MEL007, respectively. Ipi: ipilimumab; mths: months; PR: partial response.

(B) Tumor-volume-curve for MEL006 with 18 mice exposed to BRAF/MEK inhibitors until resistance (upper panel). Tumor-volume-curve for MEL015 with 6 mice exposed to BRAF/MEK inhibitors until resistance (lower panel).

(C) Mechanisms of MAPK signaling reactivation detected by targeted DNA sequencing (TruSight Tumor 26) in PDX samples (n = 10) analyzed at phase 3 (drug-resistance).

(D) Single-cell logR copy number landscapes of untreated (95) and treated (84) MEL006 PDX tumors. Thresholds for coloring were manually set based on the LogR distribution.

(E) FISH analysis for centromeric probes of chromosome 2 (CEP2) and 3 (CEP3) using treatment naive MEL006 cells cultured *in vitro* (upper panel). FISH analysis for centromeric probes of chromosome 2 (CEP2) using PDX tissue sections before treatment (T0) and during MRD (phase 2) (lower panel).

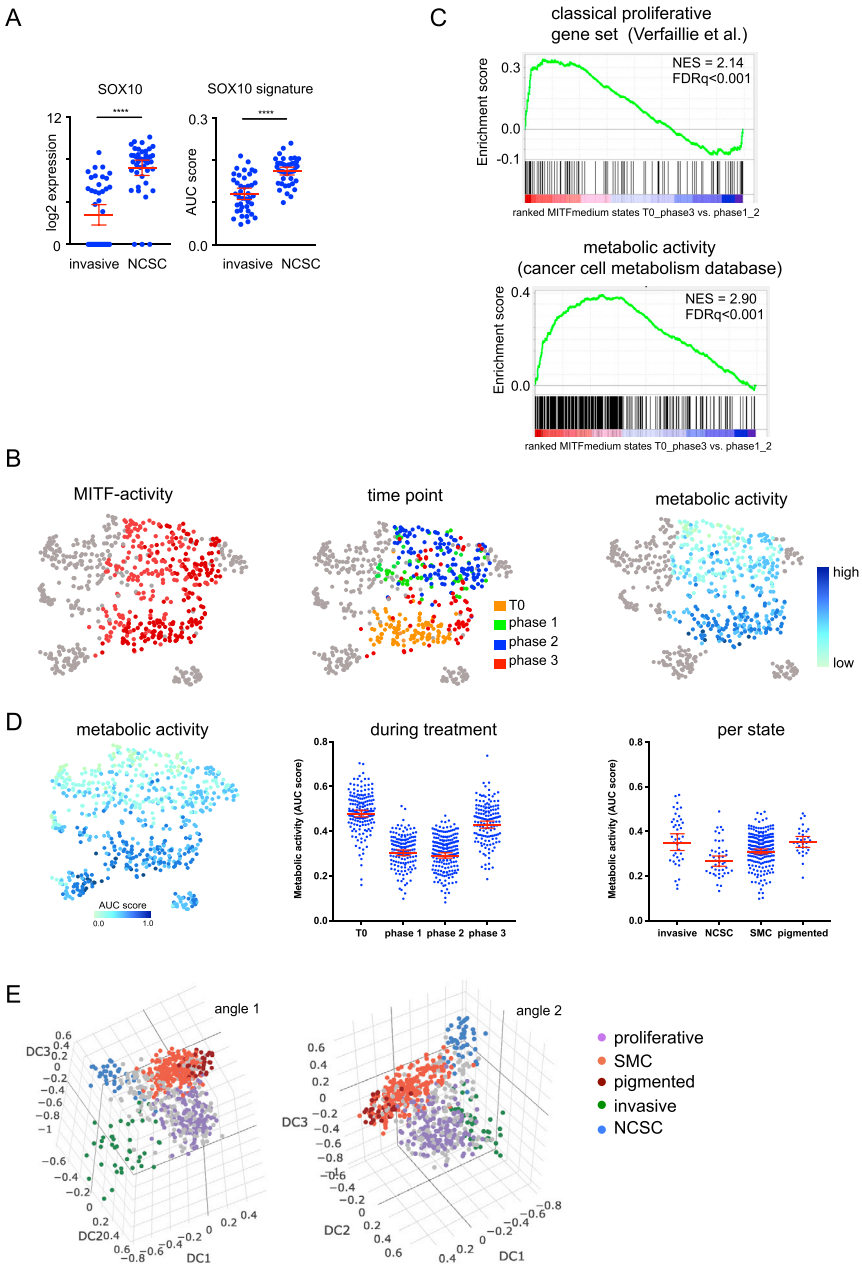

Figure S2. Cell-State Transitions during BRAF&MEK Inhibition, Related to Figure 2

(A) Quantification of SOX10 and SOX10 signature expression in the invasive and NCSC drug tolerant states. Error bars represent 95% confidence intervals, ****p < 0.0001, Mann-Whitney test.

(B) Two distinct MITF states of medium expressional activity are distinguishable. They differ by time and metabolic activity. MITF-medium cells of T0 and phase 3 are metabolically more active compared to phase 1 and 2 cells.

(C) MITF medium cells of T0 and phase 3 show significant enrichment for the classical proliferative and metabolically active signature compared to phase1&2 MITF medium cells, as shown by gene set enrichment analysis.

(D) The metabolic signature activity was quantified in each cell during the different phases of treatment and per state using AUCell.

(E) Diffusion map of proliferative, SMC, invasive, NCSC and pigmented cells.

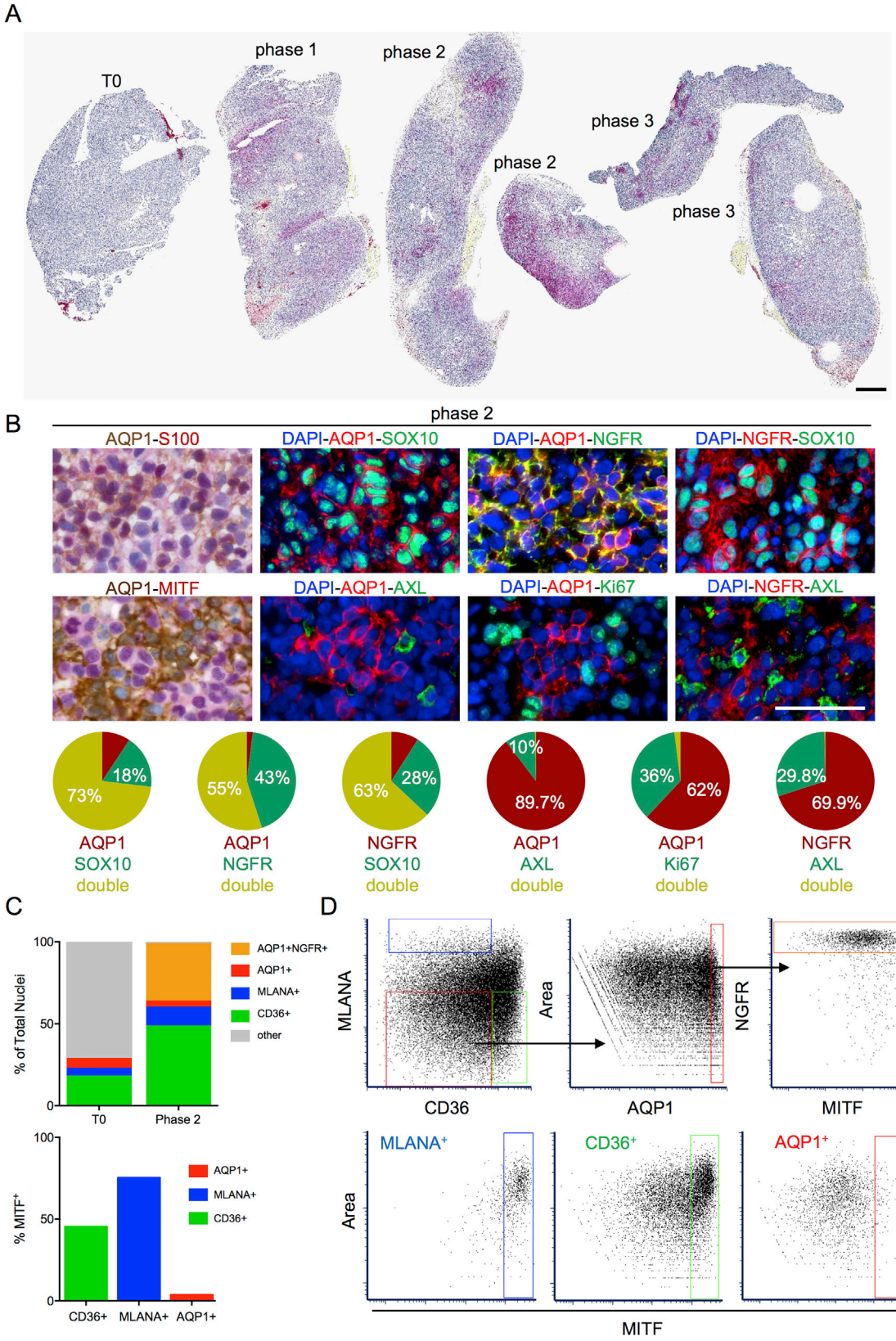

(legend on next page)

Figure S3. Enrichment of the NCSC State in MRD from MEL006, Related to Figure 3

(A) AQP1 immunostainings shown at low magnification (scale bar equals 1 mm) at T0, phase 1, 2 and 3 in MEL006.

(B) Double immunostainings for a number of NCSC and invasive markers. Scale bar equals 50 μm. The quantification of the immunostainings is shown in the lower panel. Five high power fields were counted to represent the mean percentages for single (red or green) and double positive cells (yellow). Double negative cells (DAPI only) were not taken into account.

(C) Quantification based on sequential chromogenic immunohistochemistry of the different drug-tolerant states (upper panel) and correlation with MITF expression (lower panel).

(D) Representative image cytometry plots and gating strategy for identification of MLANA+CD36-, CD36+MLANA-, AQP1+NGFR+CD36-MLANA- subpopulations in tumors on treatment (phase 2/MRD). The lower panel details image cytometry plots and intensity threshold for MITF expression on each population gated in top panel.

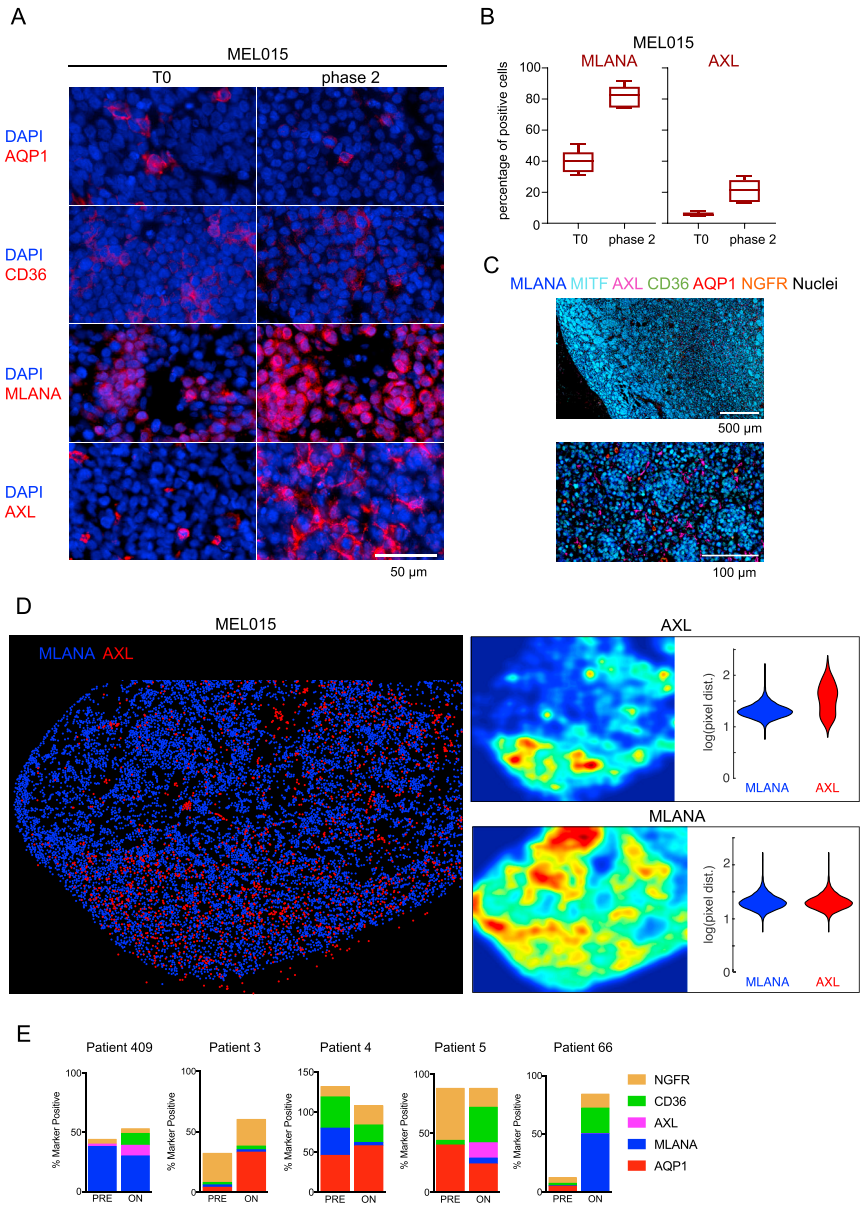

Figure S4. Characterization of MEL0015 MRD, Related to Figure 4

(A) Immunostainings of PDX model MEL015 before treatment (T0) and at phase 2 showing an increase in pigmented and invasive cell populations as revealed by markers MLANA and AXL, respectively. There was no consistent increase in AQP1 and CD36 positive cells.

(B) Quantification of cells strongly positive for MLANA and AXL as shown in A at T0 and MRD/phase 2 with five high power fields counted in each condition.

(C) Sequential chromogenic immunohistochemistry of MEL015 at phase 2 showing a predominant increase in pigmented and invasive populations based on their identification with the MLANA and AXL markers.

(D) Cell density and distribution plots for MEL015 showing dispersion of AXL positive cells in MLANA positive clusters.

(E) Percentage of cells positive for each of the five independently counted markers after staining with sequential chromogenic immunohistochemistry.

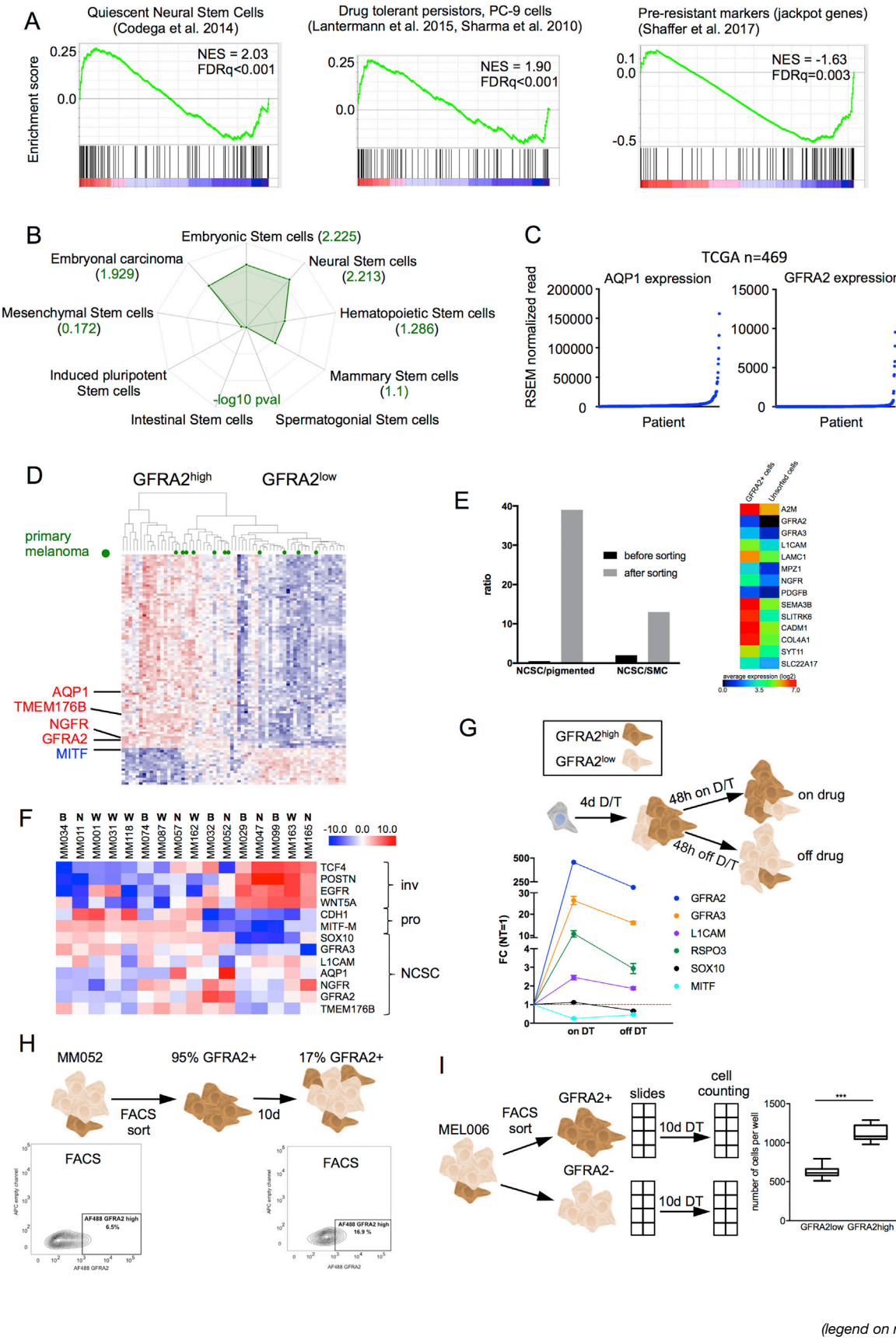

(legend on next page)

Figure S5. Transition into the Neural Crest Stem Cell-like Transcriptional State Is Reversible, Related to Figure 5

(A) GSEA plots show significant enrichment for quiescent Neural stem cells and drug tolerant persistors across the single-cell *in vivo* NDTC state.

(B) Top200 NDTC-genes were analyzed with stemchecker (Pinto et al., 2015). The spiderchart shows enrichment for embryonic and neural Stem cells

(C) AQP1 and GFRA2 expression is only detectable in a small fraction of human melanoma patients (TCGA).

(D) Additional neural genes are co-expressed with GFRA2 and anticorrelated with MITF as suggested by differential gene expression analysis of n = 32 $GFRA2^{high}$ versus n = 32 $GFRA2^{low}$ melanoma patients.

(E) scRNA-seq of FACS-sorted GFRA2 positive cells shows a strong enrichment for cells in the NCSC state (left panel) and upregulation of expression of most NCSC markers (heatmap, right panel).

(F) Heatmap shows a selection of invasive, proliferative and NDTC markers across different melanoma short term cultures. Gene expression was measured using RT-qPCR. (B = BRAFmut, N = NRASmut, W = neither B nor N).

(G) An increase in NCSC markers as assessed by qPCR was observed after 4 days of treatment with dabrafenib-trametinib. A progressive decrease in expression was observed 2 days after drug-removal.

(H) $GFRA2^{high}$ MM052 were sorted (left FACS plot) and subsequently plated in fresh drug-free medium. After 10 days in culture, FACS analysis indicated a five-fold decrease in the number of GFRA2 positive cells.

(I) GFRA2 positive and negative cells were sorted from a MEL006 culture and plated in dabrafenib-trametinib-containing medium for 10 days after which the number of cells were quantified. Right panel shows absolute number of cells per well (8 versus 8 wells, ***$p < 0.001$ Mann-Whitney test).

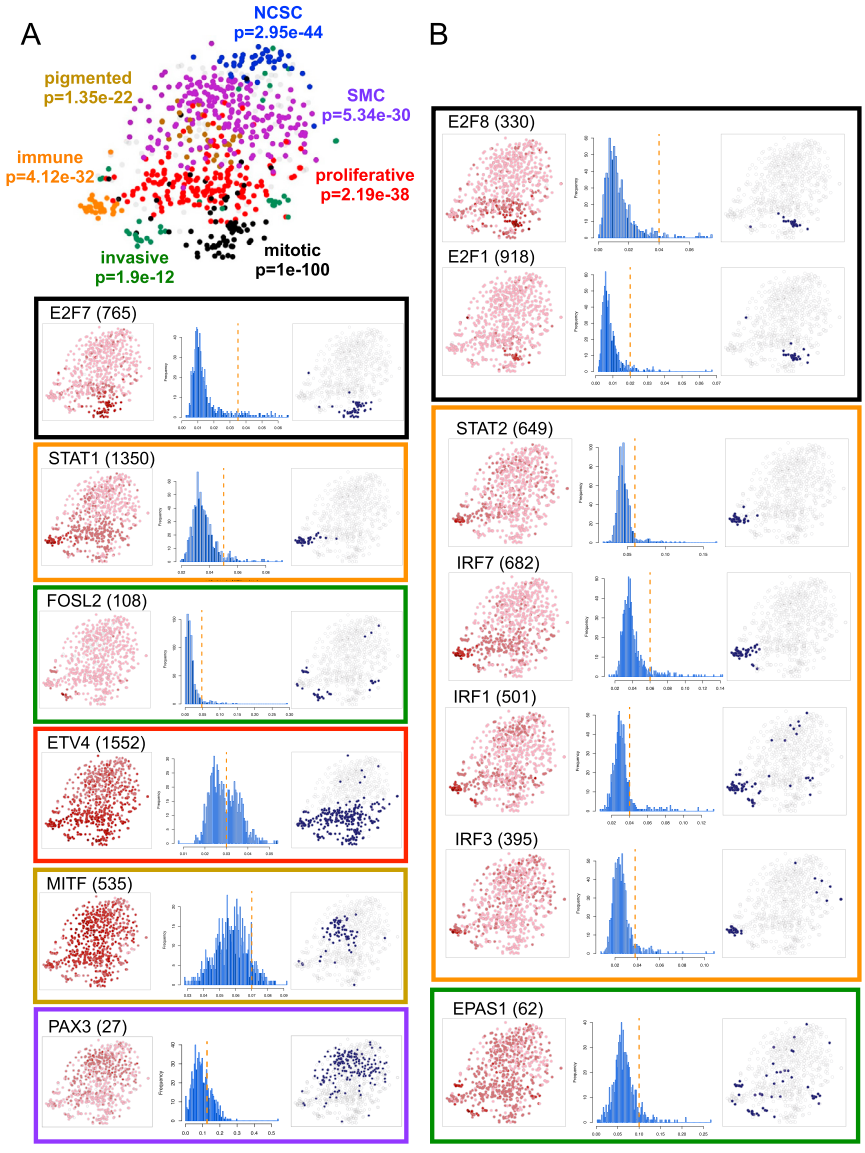

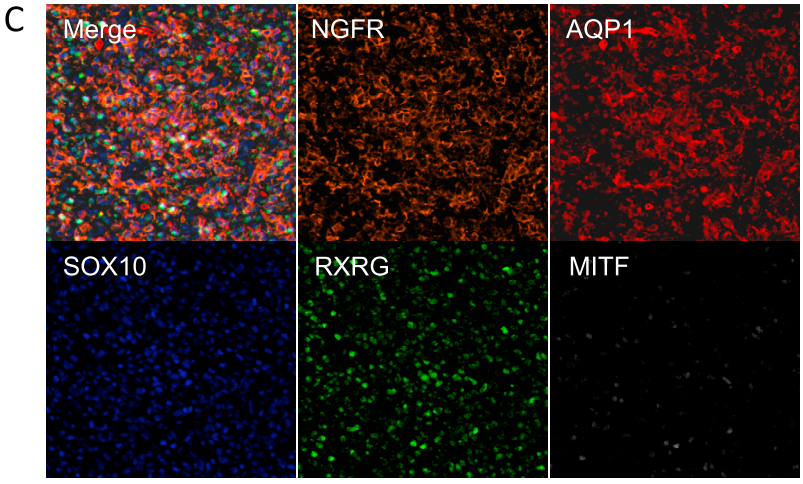

(legend on next page)

Figure S6. TF Regulon Activities and Co-expression of Drug-Tolerant State Markers, Related to Figure 6

(A) tSNE shows cells colored by state-identity (SCENIC approach). The identities are inferred by the binary activities of the TF regulons. Cell identities inferred by SCENIC are largely overlapping with the SCDE approach (****$p < 0.0001$ hypergeometric distribution test).

(B) Additional regulons of predicted transcription factors per state are shown. In the first column, AUC values are used to color the cells of the tSNE plot. The second column shows the distribution plot of AUC values together with the chosen cut-off (orange dashed line). The tSNE plot in the third column shows cells being in a higher state compared to the rest (blue). These are the cells to the right of the dashed line in the histogram. This selection constitutes the binary activity matrix.

(C) Sequential chromogenic immunohistochemistry analysis of MEL006 at MRD showing the co-expression of NGFR, AQP1, SOX10 and RXRG in cells that do not express MITF.

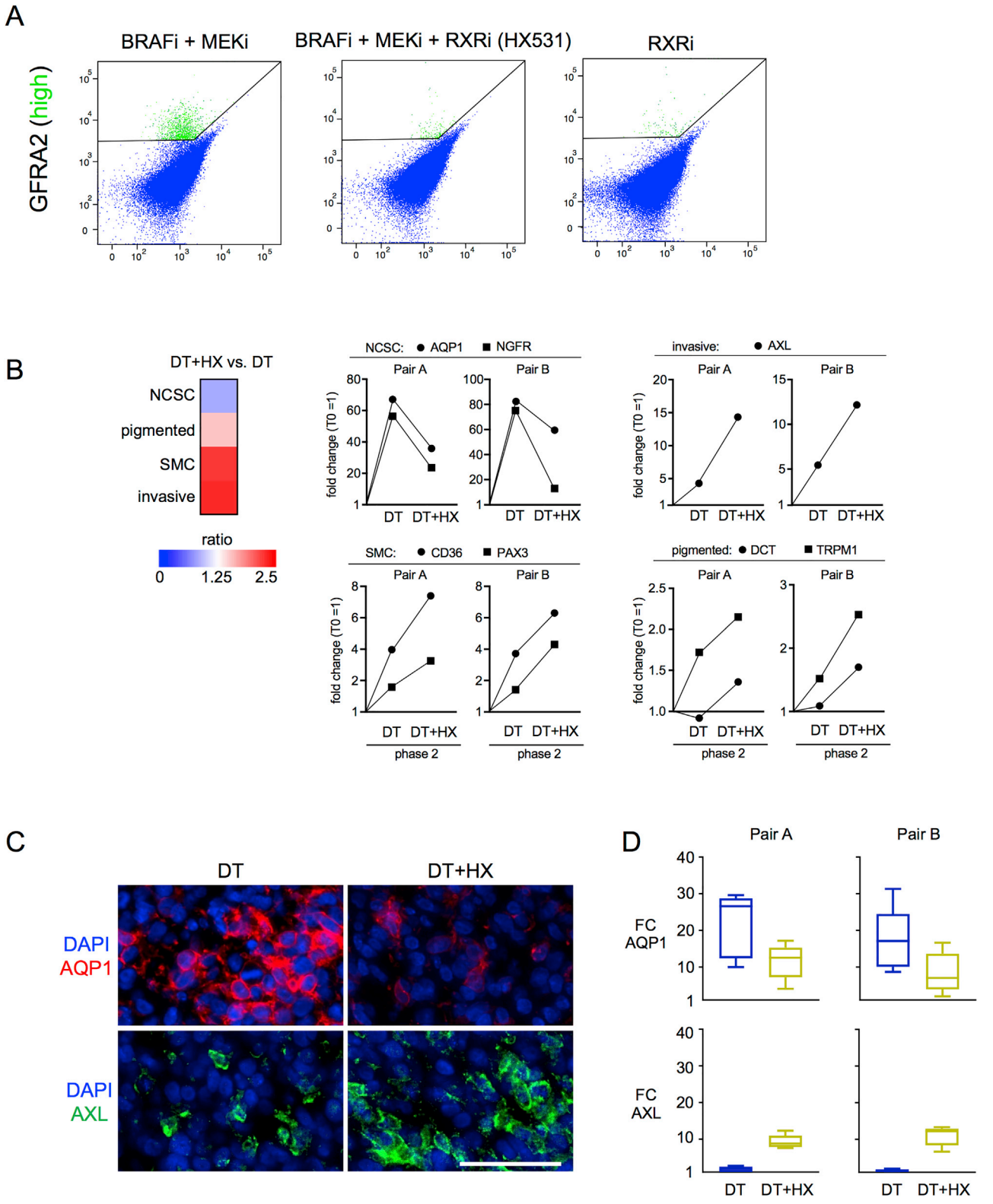

(legend on next page)

Figure S7. Perturbation of the RXR Node, Related to Figure 7

(A) Representative FACS profiles of GFRA2 positive cells after exposure to dabrafenib-trametinib and/or the RXR antagonist HX531.

(B) RT-qPCR analysis of MEL006 MRD isolated from mice treated with dabrafenib-trametinib versus dabrafenib-trametinib+HX. Heatmap shows that RXR antagonist HX531 (HX) induced a decrease in markers of the NCSC state, while expression of the other drug-tolerant states was upregulated. Relative expression (fold change) of selected markers of the NCSC (AQP1, NGFR), invasive (AXL), SMC (CD36, PAX3) and pigmented (DCT, TRPM1) subpopulations is shown in representative pairs of mice (pair A and B). Levels of expression at T0 of these markers was set to 1.

(C) Representative immunostainings for AQP1 (upper panel) and AXL (lower panel) for MEL006 at MRD isolated from mice treated with dabrafenib-trametinib (left) versus dabrafenib-trametinib+HX (right).

(D) Quantification of the immunostainings presented in D. FC denotes fold change of the number of positive cells at phase 2 relative to untreated mice (T0) with five high power fields counted in each condition.